The Astrophysical Journal, 775:131 (19pp), 2013 October 1 doi:10.1088/0004-637X/775/2/131

EVIDENCE OF HOT HIGH VELOCITY PHOTOIONIZED PLASMA FALLING ON ACTIVELY ACCRETING T TAURI STARS

Ana Ines Gómez de Castro
Grupo de Investigación Complutense AEGORA and S.D. Astronomía y Geodesia, Fac. de CC Matemáticas, Universidad Complutense, E-28040 Madrid, Spain
Received 2012 August 11; accepted 2013 July 30; published 2013 September 16

ABSTRACT

The He II (1640 Å) line and the resonance doublet of N V (UV1) provide a good diagnostic tool to constrain the excitation mechanism of hot ($T_e > 40{,}000$ K) atmospheric/magnetospheric plasmas in T Tauri stars (TTSs). Making use of the data available in the *Hubble Space Telescope* archive, this work shows that there are at least two distinct physical components contributing to the radiation in these tracers: the accretion flow sliding on the magnetosphere and the atmosphere. The N V profiles in most sources are symmetric and at rest with respect to the star. The velocity dispersion of the profile increases from non-accreting ($\sigma = 40$ km s^{-1}) to accreting ($\sigma = 120$ km s^{-1}) TTSs, suggesting that the macroturbulence field in the line formation region decreases as the stars approach the main sequence. Evidence of the N V line being formed in a hot solar-like wind has been found in RW Aur, HN Tau, and AA Tau. The He II profile has a strong narrow component that dominates the line flux; the dispersion of this component ranges from 20 to 60 km s^{-1}. Current data suggest that both accretion shocks and atmospheric emission might contribute to the line flux. In some sources, the He II line shows a broad and redward-shifted emission component often accompanied by semiforbidden O III] emission that has a critical electron density of $\sim 3.4 \times 10^{10}$ cm^3. In spite of their different origins (inferred from the kinematics of the line formation region), N V and He II fluxes are strongly correlated, with only the possible exception of some of the heaviest accretors.

Key words: magnetic fields – stars: pre-main sequence

Online-only material: color figures

1. INTRODUCTION

Solar-like pre-main-sequence (PMS) stars and, in general, low mass PMS stars ($M_* < 2M_\odot$), or T Tauri stars (TTSs), are complex dynamical systems made of two basic components, star and accretion disk, as well as a dynamical interface, the stellar magnetosphere (see Gómez de Castro 2013 for a recent review). Magnetic fields of few kG have been detected on the surface of the TTSs (Guenther et al. 1999; Johns-Krull et al. 1999; Johns-Krull 2007). The surface field is not bipolar, but like the Sun's field, it has a rather complex structure (Johns-Krull et al. 2004). Higher-order, multi-polar components fall off more rapidly with radius than the dipolar field. Unfortunately, it is difficult to observationally track the final path followed by matter from the inner disk border to the stellar surface. In addition, the magnetosphere has its own dynamics and force due to the interaction with the disk.

Unfortunately, the characteristics of the TTSs' extended atmosphere and magnetospheres are still escaping diagnosis (see Hartmann 2009). Little is known about them, apart from having a density of $\sim 10^9$–10^{11} cm^{-3} and an electron temperature between some few thousand Kelvin and 100,000 K (Gómez de Castro & Verdugo 2007, hereafter GdCV2007). Recent attempts to derive the magnetospheric properties from optical lines have shown that the Hα profile, for instance, is strongly dependent on densities and temperatures assumed inside the magnetosphere and in the disk wind region (Lima et al. 2010). The line widths of typical atmospheric/magnetospheric tracers are about 200–300 km s^{-1}, which far exceed those expected from thermal or rotational broadening even if the lines are assumed to be formed in a magnetosphere that extends to some 4–5 stellar radii and corotates with the star. As of today, it is still unclear whether the broadening is produced by unresolved macroscopic flows or by magnetic waves propagating on the magnetospheric field (Hartmann et al. 1982). In general, the broadening of magnetospheric tracers does not vary significantly in time, indicating that the average motions are rather stable. The combined effect of funnel flows and inclined magnetic rotators as simulated by Romanova et al. (2004, 2012) is the current baseline for the numerical simulation of TTSs magnetospheres. The stellar field is assumed to be anchored in the inner part of the disk, which creates a sheared layer between the rigid body rotation of the star and the Keplerian rotation of the disk. This interaction has a profound influence on the star and the accretion flow and also acts as a dynamo that transforms part of the angular momentum excess in the inner disk into magnetic field amplification. This amplification self-regulates through both quiescent periods of field build up and eruptions when the energy excess is released (see Gómez de Castro & von Rekowsky 2011 for an evaluation of the ultraviolet (UV) output from such an interaction). However, magnetospheric heating processes are poorly known, and accretion shock models are unable to predict the observed line fluxes/broadening (Johns-Krull 2009).

From the observational point of view, the TTSs are split into two groups: stars with noticeable accretion, the classical TTSs (CTTSs), and weak-line TTSs (WTTSs) where accretion signatures in the spectrum are negligible or absent. The atmospheric and magnetospheric energy output in both types is released mainly in the UV. The richness of spectral tracers for a broad range of magnetospheric temperatures and densities is unmatched by any other range. There are several studies of the atmospheric/magnetospheric properties of the TTSs based on low-dispersion UV data (Lemmens et al. 1992; Huélamo et al. 1998; Johns-Krull et al. 2000; Yang et al. 2012; Gómez de Castro & Marcos-Arenal 2012, hereafter GdCMA2012).

However, only the Cosmic Origins Spectrograph (COS) (see Green et al. 2012 for a description of the instrument) on board the *Hubble Space Telescope* (*HST*) has been sensitive enough to gather high signal-to-noise ratio (S/N) profiles of hot plasma tracers, such as the N v [UV1] resonance multiplet or the He II Hα transition, with a resolution above 10,000 in late K- and M-type TTSs (see Penston & Lago 1983 for C IV profiles obtained with the *IUE*; Ardila et al. 2002 for *HST* profiles obtained with the Goddard High Resolution Spectrograph (GHRS); and Ayres 2005 for the CoolCat set based on *HST* data obtained with the Space Telescope Imaging Spectrograph (STIS) and compare them with those presented in Section 2). Previous instruments only allowed us to observe bright or nearby sources such as TW Hya (Herczeg et al. 2002).

Following a previous work where the magnetospheric properties of TTSs were examined based on low dispersion *HST* data (GdCMA2012), the high resolution profiles of the N v [UV1], O III], and He II (1640 Å) transitions are analyzed in this work with two main objectives. First, we intend to determine whether it is feasible to discriminate the contributions to the high energy radiation flux from the high density atmospheric plasma and the accretion flow. Second, we reexamine the unexpected correlation between X-ray flux and the high energy UV tracers found by GdCMA2012 in the light of the kinematic information contained in the high resolution *HST*/COS profiles. In Section 2, the observations are described and the results are presented in Section 3. Two components are found to contribute to the He II flux: a low density component (LDC) associated with the accretion flow and a high density component (HDC) of more uncertain origin. The discussion on the possible source of the HDC, its association with accretion shocks, and the properties of the LDC are addressed in Section 4. The work concludes with a brief summary on the relevance of these results.

2. *HUBBLE SPACE TELESCOPE* OBSERVATIONS

The He II profiles of TTSs in the Taurus–Aurigae star-forming region have been retrieved from the *HST* archive. Only high resolution observations have been considered. Most of them have been obtained with the COS and the gratings G130M and G160M. The resolution is ∼24,000, and each target has been observed three times, with slight offsets in the wavelength range to guarantee that the 18.1 Å gap between the two segments in the FUV detector is covered (see COS Handbook). Moreover, a few TTSs have been observed with the STIS, namely, T Tau, DR Tau, and DF Tau. Only the T Tau profile had a high enough S/N in the He II line to be considered for this work. The log of the observations is provided in Table 1. Additional information on the *HST* programs that obtained these observations (programs IDs 11533, 11616, and 8627) can also be found in the table.

The observational strategy allowed us to search for variations in the profiles on time scales of ∼20 minutes, but neither flux nor morphology were found to display significant changes. The one-dimensional spectra produced by the COS calibration pipeline (CALCOS v2.17.3) were aligned and co-added.[1] COS targets were centered to within 0.1–0.2 arcsec to achieve the nominal wavelength accuracy of ±15 km s^{-1}. The (R(3) 1–7) 1489.636 Å and (P(5) 1–7) 1504.845 Å H_2 lines were used to set the zero of the wavelength scale for the targets in Table 1. H_2 emission was dominated by the molecular disk around the stars in most sources (France et al. 2012). The lines were selected to be strong (from Herczeg et al. 2002) and detectable in most of the sources. The profiles of the 1489.636 Å line were plotted in Figure 1 (see also Figure 3 in France et al. 2012) and the He II profiles were plotted in Figure 2. No shifts were applied to the DN Tau and IP Tau observations because the H_2 emission was too weak to be used for this purpose. Shifts were also not applied to HBC 427, LkCa 19, and LkCa 4 because H_2 emission was not detected. The H_2 profiles are sometimes asymmetric with respect to the rest wavelength, particularly in RW Aur. In this case, the original zero from the CALCOS pipeline has been left. Only a subset of AA Tau observations was used since guide star acquisition failed (see Figure 3). As a result, the first two exposures produced similar profiles while the last one produced a slightly broader and more red-shifted (by ∼0.1 Å or 18 km s^{-1} at 1640 Å) profile. For this star, the last observation was rejected and only the two first observations were averaged to produce the profiles in Figures 1 and 2.

The He II profiles can be generically described as composed of a bright and narrow emission feature and a broad, weaker component that differs from one star to another. Notice that the He II lines are very strong; this fact, together with the strong H_2 emission, contributes to the continuum jump in the low resolution Advanced Camera System on *HST* reported by GdCMA2012.

Close to the He II line, there are the O III]$_{1665}$ intercombination lines; a doublet with components at λλ1660.802 and 1666.156, which originate under transitions from the level $2s2p^3\ ^5S_2$ to the term $2s^22p^2\ ^3P$ with $J = 1$ and $J = 2$, respectively. The components should have an intensity ratio ≃1:3, equal to the ratio of their transition probabilities (145 s^{-1} and 426 s^{-1}). The transition is optically thin to a critical density of 3.4×10^{10} cm^{-3}. The O III] profiles are represented in Figure 4. The two lines of the multiplet are observed in DF Tau, HN Tau, DR Tau, SU Aur, and RW Aur; however, the flux of the weakest line 1660.802 Å, has only been measured for strong sources. In all cases, the flux ratio between the two lines of the multiplet is 1:3 (within the error bars).

To complete the view on the distribution of hot plasma in the TTSs environment, the profiles of the resonance UV 1 multiplet of the N v have also been retrieved from the *HST* archive (see Table 2). In the blue edge of the 1238.8 Å line, the strongest in the doublet, there are some narrow emission lines produced by molecular hydrogen (lines λ1237.918 1–2 P(8) and λ1237.589 2–2 R(11)) that blur the profile somewhat. The zero of the wavelength scale has been set again, resourcing to H_2 emission lines. The (P(2) 0–4) 1338.63 Å line has been used for this purpose since it is strong in most of the stars and not blended with other features (see Figure 5 with the H_2 profiles). As mentioned above, the original zero of the wavelength scale has not been shifted for DN Tau, IP Tau, HBC 427, LkCa 19, and LkCa 4 because the H_2 lines were either very weak or absent. The N v profiles can be most generally described by a single component that ranges from being narrow in stars like HBC 427, LkCa 19, and LkCa 4 to being broad and asymmetric in AA Tau or GM Aur (see Figure 6).

Some relevant properties of the TTSs used in Section 3 are gathered in Table 3. Notice that there are wide variations in published values of important parameters such as the stellar luminosity or the extinction (also see comments in GdCMA2012); data in Table 3 are gathered for reference for other researchers. The X-ray fluxes have been retrieved from the *XMM-Newton*

[1] Note that there are small wavelength windows in the spectra without flux measurements. This effect has been taken into account in the calculation of the average spectra from the three observations typically obtained per star.

Table 1
HST/COS Observations of the He II Line

Star	Instrument/ Grating	Observation ID	Start Time (yyyy-mm-dd hh:mm:ss)	Exposure Time (s)	Spec. Initial Wavelength (Å)	Spec. Final Wavelength (Å)
SU Aur[a]	COS/G160M	LB6B11010	2011-03-25 08:01:38	622.144	1387.748	1748.301
	COS/G160M	LB6B11020	2011-03-25 08:15:08	622.144	1410.706	1771.310
	COS/G160M	LB6B11030	2011-03-25 09:06:57	515.008	1434.646	1795.304
T Tau[b]	STIS/E140M	O5E304020	2000-09-08 09:11:01	2630.173	1140.000	1735.000
	STIS/E140M	O5E304040	2000-09-08 10:56:04	2320.191	1140.000	1735.000
	STIS/E140M	O5E304050	2000-09-08 12:23:56	2630.185	1140.000	1735.000
	STIS/E140M	O5E304060	2000-09-08 14:00:24	2630.164	1140.000	1735.000
LkCa 19[a]	COS/G160M	LB6B28030	2011-03-31 01:21:43	630.112	1387.740	1748.270
	COS/G160M	LB6B28040	2011-03-31 02:33:25	630.112	1410.699	1771.292
	COS/G160M	LB6B28050	2011-03-31 02:47:03	630.112	1434.577	1795.224
GM Aur[a]	COS/G160M	LB6B01030	2010-08-19 16:53:54	620.192	1387.921	1748.541
	COS/G160M	LB6B01040	2010-08-19 17:07:22	620.192	1410.957	1771.592
	COS/G160M	LB6B01050	2010-08-19 17:20:50	620.192	1431.254	1791.979
RW Aur A[a]	COS/G160M	LB6B15010	2011-03-25 02:51:01	539.008	1390.596	1751.126
	COS/G160M	LB6B15020	2011-03-25 03:03:08	538.976	1413.616	1774.208
	COS/G160M	LB6B15030	2011-03-25 03:15:43	538.976	1431.426	1792.083
HN Tau[a]	COS/G160M	LB6B09010	2010-02-10 12:49:14	1736.352	1388.187	1755.142
	COS/G160M	LB6B09020	2010-02-10 14:11:51	1396.160	1411.659	1772.251
	COS/G160M	LB6B09030	2010-02-10 15:32:12	1396.160	1435.611	1796.256
UX Tau A[a]	COS/G160M	LB6B13030	2010-12-12 14:44:10	647.168	1387.800	1748.355
	COS/G160M	LB6B13040	2010-12-12 14:58:03	647.104	1410.723	1771.317
	COS/G160M	LB6B13050	2010-12-12 15:11:58	647.200	1434.591	1795.276
HBC 427[a]	COS/G160M	LB6B26030	2011-03-30 02:34:43	644.992	1387.800	1748.355
	COS/G160M	LB6B26040	2011-03-30 02:48:36	645.120	1410.881	1771.450
	COS/G160M	LB6B26050	2011-03-30 03:02:29	645.088	1434.662	1795.309
AA Tau[a]	COS/G160M	LB6B07010	2011-01-06 20:30:32	1418.176	1387.834	1748.363
	COS/G160M	LB6B07020	2011-01-06 21:40:00	1387.168	1410.854	1771.435
	COS/G160M	LB6B07030	2011-01-06 22:06:15	1387.136	1434.611	1795.257
DR Tau[a]	COS/G160M	LB6B14010	2010-02-15 11:08:53	582.016	1388.651	1749.265
	COS/G160M	LB6B14020	2010-02-15 12:04:39	581.952	1411.842	1772.470
	COS/G160M	LB6B14030	2010-02-15 12:17:29	581.984	1435.647	1796.340
LkCa 4[a]	COS/G160M	LB6B27030	2011-03-30 07:32:26	600.192	1387.798	1748.330
	COS/G160M	LB6B27040	2011-03-30 07:45:34	600.160	1410.781	1771.352
	COS/G160M	LB6B27050	2011-03-30 07:58:42	600.128	1434.635	1795.284
V836 Tau[a]	COS/G160M	LB6B06010	2011-02-05 05:06:58	1480.192	1393.645	1754.155
	COS/G160M	LB6B06020	2011-02-05 06:12:31	1391.136	1410.840	1771.423
	COS/G160M	LB6B06030	2011-02-05 06:38:50	1391.200	1434.670	1795.307
DE Tau[a]	COS/G160M	LB6B08030	2010-08-20 15:14:30	617.152	1387.865	1748.487
	COS/G160M	LB6B08040	2010-08-20 15:27:55	617.184	1410.962	1771.598
	COS/G160M	LB6B08050	2010-08-20 15:41:20	617.088	1434.735	1795.449
IP Tau[a]	COS/G160M	LB6B05010	2011-03-21 08:11:35	1179.136	1393.598	1754.105
	COS/G160M	LB6B05020	2011-03-21 09:15:35	972.192	1407.600	1768.179
	COS/G160M	LB6B05030	2011-03-21 09:34:45	972.128	1440.509	1801.117
DF Tau[c]	COS/G160M	LB3Q020A0	2010-01-11 13:07:29	1324.192	1435.545	1796.229
	COS/G160M	LB3Q02090	2010-01-11 12:00:02	1408.192	1423.424	1784.071
	COS/G160M	LB3Q02080	2010-01-11 11:32:10	1408.192	1411.793	1772.421
	COS/G160M	LB3Q02070	2010-01-11 10:24:56	1408.192	1400.406	1761.021
DM Tau[a]	COS/G160M	LB6B02030	2010-08-22 17:23:51	978.176	1387.890	1748.500
	COS/G160M	LB6B02040	2010-08-22 18:26:31	1396.128	1410.865	1771.514
	COS/G160M	LB6B02050	2010-08-22 18:52:45	1396.160	1434.871	1795.561
DN Tau[a]	COS/G160M	LB6B04030	2011-09-10 18:14:50	965.120	1435.325	1796.015
	COS/G160M	LB6B04040	2011-09-10 18:34:41	1387.136	1387.879	1748.477
	COS/G160M	LB6B04050	2011-09-10 19:50:39	1387.168	1411.111	1771.74
UZ Tau[d]	COS/G160M	LBH208020	2011-03-06 22:48:19	1944.288	1384.094	1748.243

Notes.
[a] Observations obtained under *HST* proposal 11616 on "The disks, accretion, and outflows of TTSs" with PI: Gregory Herczeg.
[b] Observations obtained under *HST* proposal 8627 on "Testing the theories of wind/jet production in YSOs" with PI: Nuria Calvet.
[c] Observations obtained under *HST* proposal 11533 on "Accretion flows and winds of PMS stars" with PI: James Green.
[d] Observations obtained under *HST* proposal 12161 on "Accretion in close pre-main-sequence binaries" with PI: David Ardila.

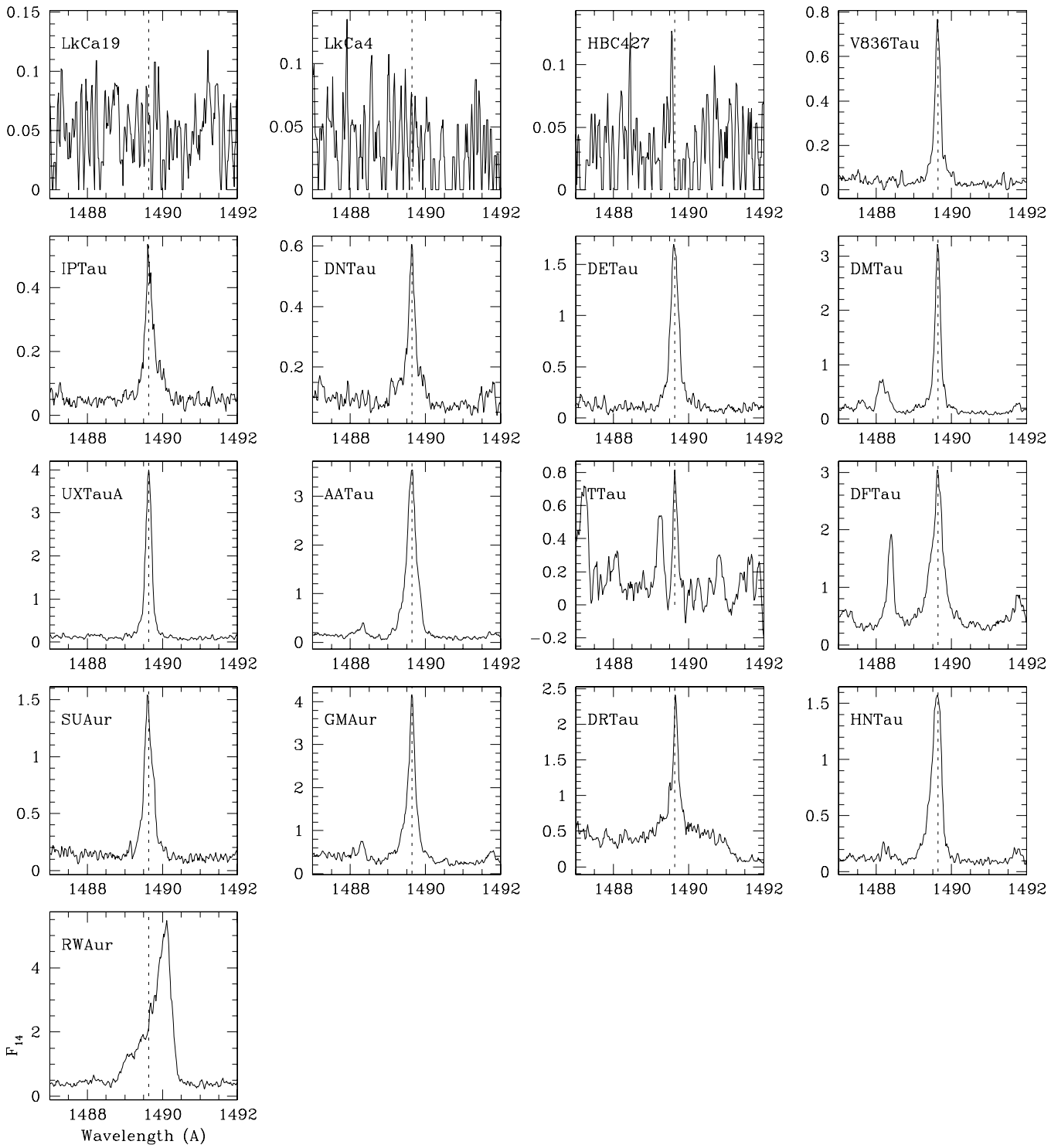

Figure 1. Profiles of the (R(3) 1–7) 1489.636 Å H_2 line of the TTSs studied in this work. The zero of the wavelength scale is set using H_2 lines for reference (see text). Notice the asymmetry and broadening of the RW Aur profile which prevent its use for this purpose. Fluxes are given in units of 10^{-14} erg s^{-1} cm^{-2} Å^{-1} (F_{14}).

extended survey of the Taurus (XEST) molecular cloud (Güdel et al. 2007). The He II, 1238.82 Å N V, and the O III] line fluxes have been measured after subtracting the local continuum. Also the fluxes for the 1489.636 and 1338.63 H_2 lines have been measured (see Section 5). The line fluxes are provided in Table 4; they are not extinction corrected. For some sources, the measurement of the 1238.82 Å N V flux has required subtracting the nearby H_2 features. In such cases, the H_2 flux has been subtracted by linear interpolation in the N V profile. However, there are a few profiles where this interpolation was uncertain (see quality flags in Table 4).

3. RESULTS

From Figures 2, 4, and 6, a generic trend can be inferred.

1. The weak-line TTSs (WTTSs) in the sample, i.e., evolved TTSs with no evidence of mass infall (LkCa 19, LkCa 4,

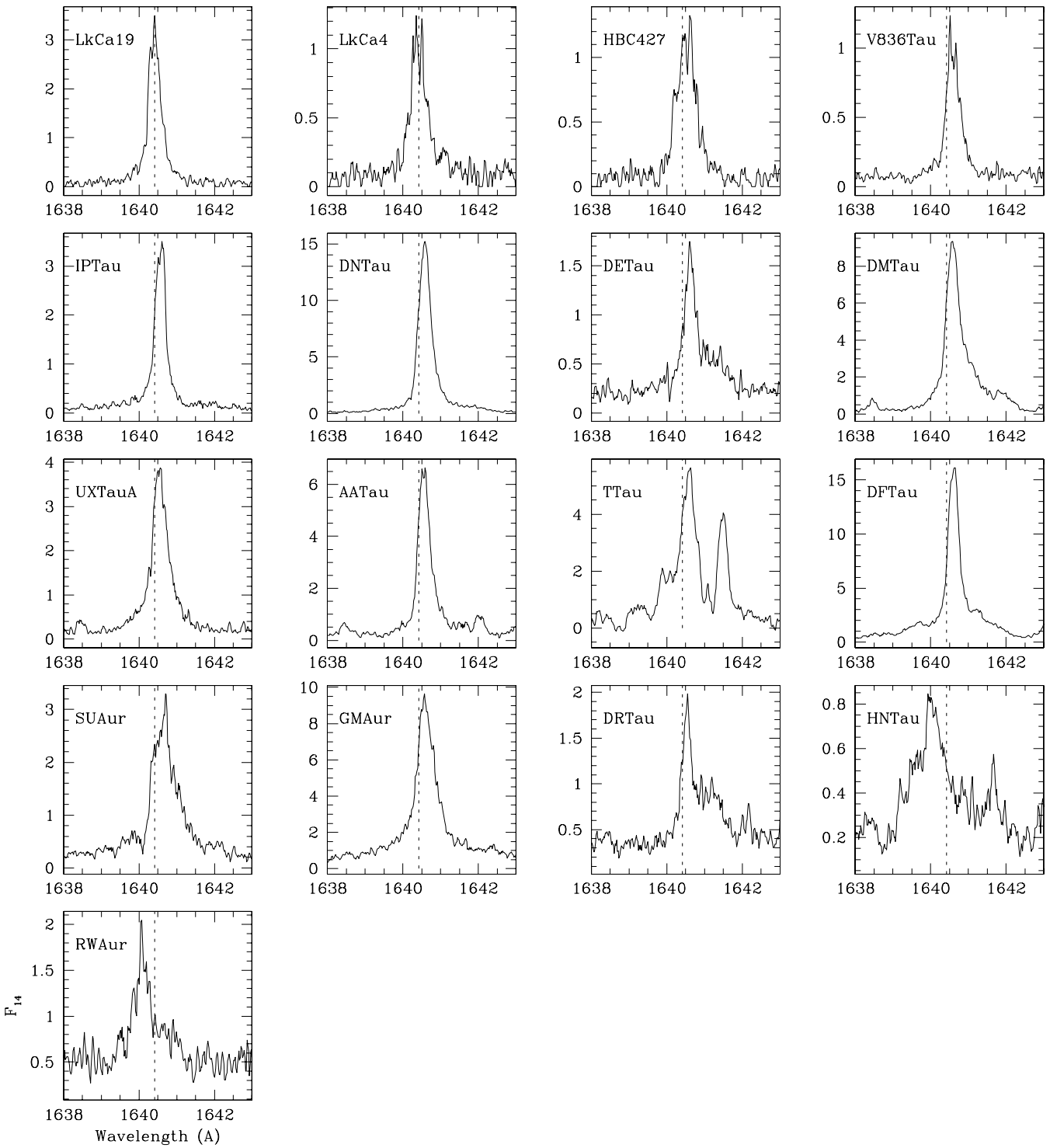

Figure 2. He II profiles of the TTSs in Taurus observed with *HST*. The rest wavelength of the He II line is marked for reference (see also Figure 1). Fluxes are given in units of 10^{-14} erg s^{-1} cm^{-2} Å^{-1} (F_{14}).

HBC 427), display neither H_2 emission nor nebular O III] emission. They have only rather narrow He II and N V lines.

2. The classical TTSs (CTTSs) emit in all these tracers (see below).
3. Some intermediate objects (TTSs), such as IP Tau, DN Tau, and V836 Tau, have weak H_2 and no nebular O III] emission. Both He II and N V lines have narrow emission profiles.

CTTSs cover a broad range of profile morphologies. Strong H_2 emission is detected in all of them, and the lines are narrow except in RW Aur A (see France et al. 2012). Nebular O III] emission is detected in all of them except DM Tau, UX Tau A, and AA Tau. O III] is especially strong in T Tau, DF Tau, HN Tau, DR Tau, and RW Aur. SU Aur and DE Tau seem to be intermediate objects. Hints of a possible O III] emission at 1666 Å are seen in GM Aur, though unfortunately the S/N is low and the weakest component of the multiplet is not detected. A low S/N feature is detected at 1666 AA in DN Tau, IP Tau, AA Tau, and UX Tau spectra. Observations of the C III] intercombination transition line are only available for three of

Table 2
COS/G130M Observations of the N v Line

Star	Observation ID	Start Time (yyyy-mm-dd hh:mm:ss)	Exposure Time (s)	Spec. Initial Wavelength (Å)	Spec. Final Wavelength (Å)
SU Aur[a]	LB6B11040	2011-03-25 09:19:35	894.048	1132.513	1433.611
	LB6B11050	2011-03-25 09:39:54	894.016	1171.264	1471.991
LkCa 19[a]	LB6B28010	2011-03-30 23:21:36	972.032	1132.687	1433.865
	LB6B28020	2011-03-31 00:57:29	972.032	1171.018	1472.086
GM Aur[a]	LB6B01020	2010-08-19 15:30:01	1064.000	1173.883	1472.056
	LB6B01010	2010-08-19 14:07:11	1064.032	1135.175	1434.068
RW Aur A[a]	LB6B15040	2011-03-25 04:20:18	881.920	1134.524	1433.479
	LB6B15050	2011-03-25 04:40:25	882.016	1171.212	1471.940
HN Tau[a]	LB6B09040	2010-02-10 17:01:25	2862.368	1172.119	1472.816
	LB6B09050	2010-02-10 18:37:17	2862.368	1133.578	1434.835
UX Tau A[a]	LB6B13010	2010-12-12 13:21:36	814.016	1132.756	1433.955
	LB6B13020	2010-12-12 13:40:33	813.976	1178.443	1472.069
HBC 427[a]	LB6B26010	2011-03-29 23:42:24	1116.000	1132.765	1433.914
	LB6B26020	2011-03-30 01:11:12	1007.040	1171.207	1472.055
AA Tau[a]	LB6B07040	2011-01-06 23:15:54	2844.320	1171.275	1471.974
	LB6B07050	2011-01-07 00:51:43	2844.352	1132.673	1433.841
DR Tau[a]	LB6B14040	2010-02-15 12:31:03	851.936	1135.968	1434.705
	LB6B14050	2010-02-15 13:40:31	852.032	1171.490	1467.855
LkCa 4[a]	LB6B27010	2011-03-30 06:05:02	1152.000	1132.813	1434.013
	LB6B27020	2011-03-30 06:29:21	1152.000	1171.085	1472.155
V836 Tau[a]	LB6B06040	2011-02-05 07:48:28	2852.384	1171.243	1471.854
	LB6B06050	2011-02-05 09:24:21	2852.384	1132.642	1433.753
DE Tau[a]	LB6B08010	2010-08-20 12:23:06	1033.984	1132.918	1431.810
	LB6B08020	2010-08-20 13:50:31	1033.984	1172.592	1472.092
DF Tau[b]	LB3Q02030	2010-01-11 07:10:07	1000.192	1136.215	1429.787
	LB3Q02040	2010-01-11 08:20:23	1001.216	1145.843	1439.456
	LB3Q02050	2010-01-11 08:40:31	1410.208	1155.476	1449.112
	LB3Q02060	2010-01-11 09:56:16	1416.192	1165.040	1458.662
IP Tau[a]	LB6B05040	2011-03-21 09:54:41	1439.360	1139.996	1433.623
	LB6B05050	2011-03-21 11:08:05	1852.384	1170.797	1467.013
DM Tau[a]	LB6B02010	2010-08-22 15:19:45	1812.384	1171.278	1472.153
	LB6B02020	2010-08-22 16:50:38	1646.336	1132.819	1434.034
DN Tau[a]	LB6B04010	2011-09-10 15:38:59	1252.320	1171.707	1472.443
	LB6B04020	2011-09-10 16:52:59	1651.360	1133.030	1434.215

Notes.
[a] Observations obtained under *HST* proposal 11616 on "Accretion flows and winds of PMS stars" with PI: James Green.
[b] Observations obtained under *HST* proposal 11533 on "The disks, accretion, and outflows of TTSs" with PI: Gregory Herczeg.

the stars in the sample, namely, DE Tau, T Tau, and RW Aur, and no significant differences have been found between the O III] and the C III] profiles obtained either with the GHRS (compare Figure 4 with Figure 1 in Gómez de Castro & Verdugo 2001) or STIS (compare Figure 4 with Figure 1 in Gómez de Castro et al. 2003).

In general, the He II profiles can be described as having a narrow emission component superimposed on a broader contribution that mimics the observed in the O III] nebular lines when high enough S/N data profiles are observed. This effect is clearly apparent in HN Tau and RW Aur (see Figure 7). Note that in DR Tau and DF Tau, the overlap is lost at blueward-shifted velocities; there is a blueward-shifted O III] emission with no He II counterpart. This blueward shifted excess could be caused by the contribution of an unresolved jet to the line emission. As shown for RY Tau by GdCV2003, the semiforbidden emission has two components, one associated with the jet and another with the accretion flow, that were disentangled for this source due to their variability. The N v profiles however, do not follow the same morphological trend. A rather narrow symmetric profile is observed in DE Tau that becomes wider in DM Tau, DF Tau, UX Tau A, GM Aur, and SU Aur, all of which are sources with absent or weak O III] nebular emission. DR Tau, HN Tau, RW Aur, and AA Tau display very peculiar profiles that clearly indicate that N v emission is not produced in the stellar atmosphere but in another dynamical component. In particular, the N v profiles of RW Aur, HN Tau, and AA Tau are asymmetric, extending from redward-shifted velocities to peak at blueward-shifted velocities; moreover, the RW Aur profile peaks at the velocity of the optical jet (Hirth et al. 1997) that was also detected in the C III] intercombination line by Gómez de Castro & Verdugo (2003). This type of profile asymmetry has also been detected in the C III] profile of RY Tau in GdCV2007, which pointed out that the line could be formed in a PMS analog of the solar wind. In this context, it is worth remarking that the H_2 profile of RW Aur has a completely different asymmetry. The flux peaks to the red of the line, suggesting the presence of infalling cold molecular gas similar to that observed in the PMS close binary AK Sco (see also Gómez de Castro et al. 2013).

These groups can be cleanly recognized in velocity dispersion diagrams. The characterization of the underlying velocity field and thermal properties of the line emission region is complex in the TTSs environment. Instead of using the standard fitting

Table 3
Main Properties of the TTSs

Object	Spectral Type	L_*[a] ($L_\odot$)	A_V[a] (mag)	$V \sin(i)$[b] (km s^{-1})	Age[a] log τ (yr)	Period (days)	L_X (10^{30} erg s^{-1})
SU Aur	G1	7.8	0.90	66.2	6.80 ± 0.08	3.5	11.641
T Tau	K0	7.8	1.8	20.1	...	2.8	9.395
LkCa 19	K0	1.56[c]	0	19	7.17 ± 0.01	2.24	...
GM Aur	K3	1.2	1.1	12.4	6.9 ± 0.2	12	0.69[e]
RW Aur	K4	1.72[c]	0.32	17.2	7.20 ± 0.11	5.4	...
HN Tau	K5	0.7[d]	0.52	52.8	...	...	0.18[e]
UX Tau	K5	1.29[c]	0.0	26	6.43 ± 0.17	...	...
HBC 427	K5Bin	2	0.6	...	...	...	6.3
AA Tau	K7	1.1	1.4	11	...	8.2	1.039
DR Tau	K7	1.7	1.0	<10.0	5.92 ± 0.2	7.3	
LkCa 4	K7	0.73[c]	0.69	26.1	6.43 ± 0.25	3.38	1.99[e]
V836 Tau	K7	0.8[e]	1.1	<15.0	...	6.76	
DE Tau	M0	1.2	1.1	10.0	...	7.6	0.025[e]
IP Tau	M0	0.7	0.9	11.0	6.6 ± 0.2	3.3	...
DF Tau	M1, M3.5	0.47, 0.53[f]	0.04	16.1	6.28 ± 0.17	8.5	...
DM Tau	M1	0.35	0.6	10	6.87 ± 0.34	...	1.181
DN Tau	M1	1.2	0.8	8.1	6.15 ± 0.11	6.6	1.072
UZ Tau	M1	0.31	1.0	15.9	...	...	0.736

Notes.
[a] L_*, A_V, and age as in GdCMA2012 unless otherwise indicated.
[b] Clarke & Bouvier (2000).
[c] Bertout et al. (2007).
[d] L_* in Table 1 from Ingleby et al. (2009) was too small. Kenyon & Hartmann (1995) was used instead.
[e] Yang et al. (2012).
[f] Luminosities of DF Tau A and DF Tau B are from Bertout et al. (2007).

Table 4
Measurements and Data

Object	F(He II)	F_{1666}(O III])[a]	F (N V)[b] (10^{-14} erg s^{-1} cm^{-2})	F_{1338} (H_2)	$F_{1489.636}$ (H_2)
SU Aur	2.05 ± 0.13	0.46 ± 0.18^w	0.53 ± 0.05^c	2.82 ± 0.14	0.41 ± 0.04
T Tau	4.87 ± 0.96	1.14 ± 0.41^i	...	...	...
LkCa 19	1.43 ± 0.10	...	0.22 ± 0.03^n	...	...
GM Aur	6.22 ± 0.19	...	2.17 ± 0.22^n	8.76 ± 0.67	1.08 ± 0.06
RW Aur	0.66 ± 0.12	2.10 ± 0.43^s	0.66 ± 0.11^b	6.49 ± 0.91	3.26 ± 0.15
HN Tau	1.33 ± 0.26	1.24 ± 0.26^i	0.27 ± 0.03^c	4.45 ± 0.23	1.04 ± 0.07
UX Tau	2.25 ± 0.12	...	0.88 ± 0.08^c	4.29 ± 0.21	0.85 ± 0.03
HBC 427	0.77 ± 0.10	...	0.08 ± 0.02^n	...	...
AA Tau	2.93 ± 0.06	...	0.14 ± 0.01^c	9.12 ± 0.24	1.16 ± 0.05
DR Tau	0.93 ± 0.15	2.14 ± 0.49^s	0.25 ± 0.05^c	2.33 ± 0.34	0.52 ± 0.09
LkCa 4	0.54 ± 0.06	...	0.07 ± 0.01^n	...	...
V836 Tau	0.44 ± 0.03	...	0.07 ± 0.01^c	0.45 ± 0.05	0.15 ± 0.01
DE Tau	0.87 ± 0.16	0.27 ± 0.11^i	0.35 ± 0.05^b	2.76 ± 0.28	0.45 ± 0.05
IP Tau	1.33 ± 0.04	...	0.08 ± 0.02^c	0.17 ± 0.05	0.13 ± 0.02
DF Tau	7.32 ± 0.20	1.42 ± 0.47^i	1.07 ± 0.07^b	15.9 ± 0.6	0.94 ± 0.07
DM Tau	7.28 ± 0.18	...	0.68 ± 0.10^c	6.72 ± 0.31	0.61 ± 0.03
DN Tau	6.53 ± 0.06	...	0.88 ± 0.08^n	0.88 ± 0.13	0.15 ± 0.04
UZ Tau[c]	1.06 ± 0.34	0.43 ± 0.33	...	...	0.55 ± 0.02

Notes.
[a] w, i, and s stand for weak, intermediate, and strong line, respectively. The flux in the 1660.802 Å line has only been measured for strong sources. F_{1660} is equal to $(0.34 \pm 0.23) \times 10^{-14}$ erg s^{-1} cm^{-2} for DR Tau and $(0.46 \pm 0.23) \times 10^{-14}$ erg s^{-1} cm^{-2} for RW Aur.
[b] The line flux may be affected by the H_2 feature. A quality flag is inserted. Fluxes are flagged with ^{b} (strong blends), ^{c} (clean blends where the H_2 and N V contributions can be separated), and ^{n} (no H_2 emission is detected).
[c] UZ Tau is a close binary, and observations during various phases are available. The H_2 lines' flux is constant, but He II and O III] fluxes are variable. The values provided in the table correspond to the mean and standard deviation of the measured fluxes during the cycle. During the cycle, the He II and O III] fluxes vary by a factor of three.

to Gaussian or Voight profiles, it is preferable to characterize the profile in terms of the standard Pearson statistics moments and measures, i.e., mean or centroid, dispersion, kurtosis, and skewness. They provide a quantitative measurement of the deviation of the profile from the expected for thermal plasmas, i.e., a normal distribution convolved with the line spread function of COS (Kriss 2011). Note that in this approach, the profile is assumed to be formed by the contribution to

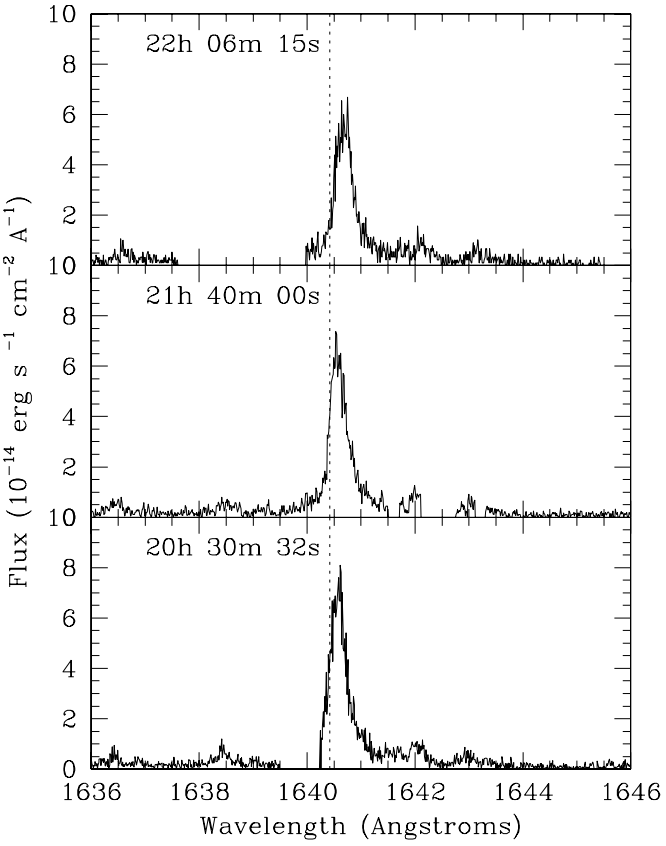

Figure 3. Three observations of the He II line in AA Tau with *HST*/COS. The rest wavelength of the He II line is marked for reference. During the observations, the guide star acquisition failed. Note the broadening and shift of the central peak from the first to the last observation.

the line flux of independent gas parcels, i.e., the (background subtracted) profile is treated as a histogram of the flux emitted per parcel in the wavelength (velocity) space; a similar approach was followed by GdCV2007 to compare the observed C III] and Si III] profiles of RY Tau with the theoretical predictions. This treatment permits the characterization of the profiles of optically thin lines formed in complex velocity fields. In Table 5, the dispersions of the He II and N V lines are provided together with those obtained for two control lines, the H_2 transitions at 1339 Å and 1489 Å. RW Aur, HN Tau, and AA Tau are not included because their N V profiles are peculiar. As shown in the bottom panel of Figure 8, the average dispersion of the H_2 profiles is 31 ± 5 km s^{-1} and 43 ± 13 km s^{-1} for the 1339 Å and 1489 Å lines, respectively. There is no correlation between the broadening of these two H_2 lines, pointing out that the scattering of the dispersions in the diagram is related to random effects associated with the measurement process. A different trend is drawn from the N V and He II dispersions. The dispersions of the WTTSs and DN Tau are comparable to those measured in the H_2 line. In intermediate objects, like V836Tau and IP Tau, the dispersions in the He II line are comparable to those measured in the H_2 lines, but the N V lines are significantly broader. Finally in the CTTSs both σ(N V) and σ(He II) are larger than $\sigma(H_2)$. Note that stellar rotation may contribute to the line dispersion; SU Aur, the fastest rotator in the sample, also has the largest dispersion. However, a large dispersion can also be produced by profile asymmetry. For instance, DM Tau has dispersions comparable to those measured in SU Aur and it is one of the slowest rotators in the sample (see Table 3). Two objects do not follow this trend: DR Tau and DE Tau, both of which have intermediate dispersions in the N V lines and large dispersions in the He II lines caused by the broad emission component. A quick inspection in the summary of the TTSs properties (see Table 3) indicates that the only possible cause of this discrepancy is the high accretion rate, as is expected.

Table 5
UV Line Profile Dispersion

Stars	$\sigma(H_2$ 1339 Å) (km s^{-1})	$\sigma(H_2$ 1489 Å) (km s^{-1})	σ(N V 1238 Å) (km s^{-1})	σ(He II) (km s^{-1})
AA Tau	52.38	33.32	89.66	40.19
DE Tau	39.61	26.72	79.97	68.05
DF Tau	52.38	36.71	116.3	48.66
DM Tau	48.51	21.8	138.1	88.85
DN Tau	48.51	39.81	36.35	39.7
DR Tau	34.3	34.49	70.27	70.34
GM Aur	65.69	30.85	123.6	62.25
HN Tau	56.01	29.54	130.9	87.04
IP Tau	19.81	33.32	72.7	32.58
SU Aur	28.01	26.72	143	63.9
UX Tau	34.3	23.55	99.35	58.41
V836 Tau	34.3	32.1	67.85	33.26
LkCa 19	...	...	33.93	41.47
LkCa 4	...	...	38.77	36.05

3.1. Two Hot Plasma Components in the TTSs

From Figures 2, 4, and 6, it is clearly inferred that there are at least two different plasmas contributing to the spectral lines under study:

1. A low-density component (LDC) that it is most conspicuously traced by the O III] line. The LDC also produces the He II broad emission component observed in RW Aur, HN Tau, DR Tau, and DF Tau. The critical density of the O III] sets an upper limit to the electron density[2] of the plasma in the LDC of $\simeq 3.4 \times 10^{10}$ cm^{-3} (also see Section 4.2). The LDC profiles display a non-thermal broadening and draw a complex velocity field around the stars. In fact, the LDC profiles seem to trace some kind of complex magnetospheric infalling pattern high above the stellar surface. Also, in some cases, they could be associated with unresolved wind structures (Gómez de Castro & Ferro-Fontán 2005), as the reported for RY Tau (GdCV2007). Notice that the co-existence of O III] and He II radiation from the same kinematic structure would point to unrealistically high electron temperatures for the line emission region ($\log T_e$ (K) $\sim$ 5.4), if collisional equilibrium at a single temperature is assumed and electron densities below the O III] critical density are considered.[3] In fact, its UV spectrum is reminiscent of that observed in photoionized nebulae (also see Section 4). To the current sensitivity, the contribution of this component to the N V flux is negligible.
2. A *high density/temperature component (HDC)* that dominates the N V emission. O III] profiles are very different from N V profiles, suggesting that the density of the N V formation region is higher than the O III] critical density.

[2] Note that for electron densities above the critical density, there may still be a line emission, though it damps rapidly.
[3] Calculations made using the Chianti data base: www.chiantidatabase.org.

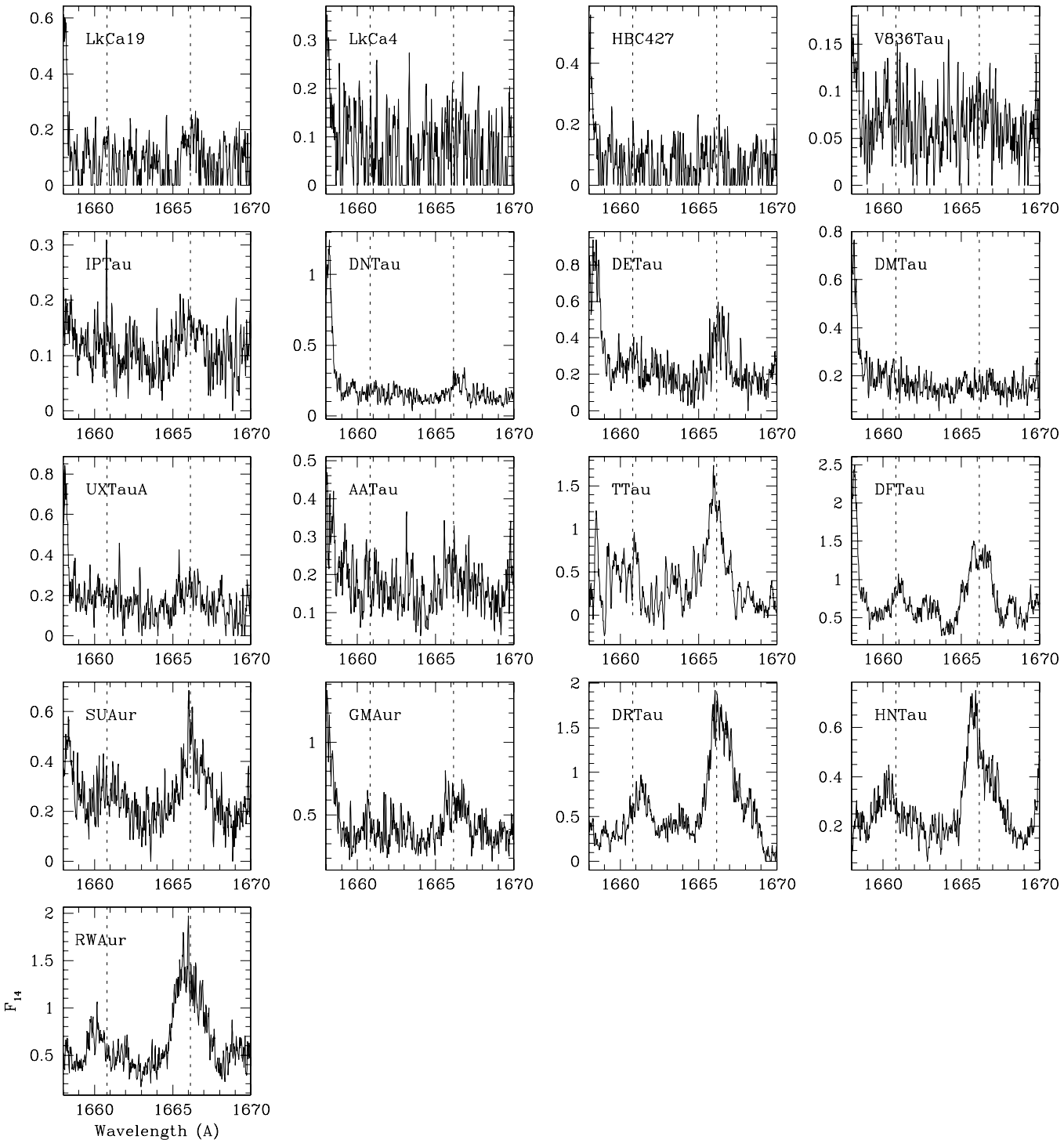

Figure 4. O III] profiles of the TTSs in Taurus observed with *HST*. The rest wavelength of the two lines in the multiplet is marked for reference (see also Table 1). Fluxes are given in units of 10^{-14} erg s^{-1} cm^{-2} Å^{-1} (F_{14}).

Though the kinematics of the N v emission region are clearly different from that traced by the LDC, the N v flux is correlated with the He II flux as shown in Figure 9. The Spearman rank correlation coefficient is $r_s = 0.87$ (with significance level, $\alpha = 0.001$, see Sachs 1982 for details), and

$$\log(F(\mathrm{He\,II})) = (0.8 \pm 0.1)\log(F(\mathrm{N\,V})) - (2.5 \pm 1.7),$$

with rms = 0.29 (see bottom panel in Figure 9). Also the fluxes normalized to the stellar surface are correlated with $r_s = 0.82$, with $\alpha = 0.002$ (see top panel in Figure 9), and

$$\log\left(\frac{F(L(\mathrm{He\,II}))}{F_{\mathrm{bol}}}\right) = (0.9 \pm 0.1)\log\left(\frac{F(\mathrm{N\,V})}{F_{\mathrm{bol}}}\right) + (0.0 \pm 0.6),$$

with an rms = 0.31. The normalized flux is defined as the rate $F_{\mathrm{He\,II}}/F_{\mathrm{bol},*}$ or $F_{\mathrm{N\,V}}/F_{\mathrm{bol},*}$ and was introduced by GdCMA2012 to provide a measure of the line emissivity weighted over an

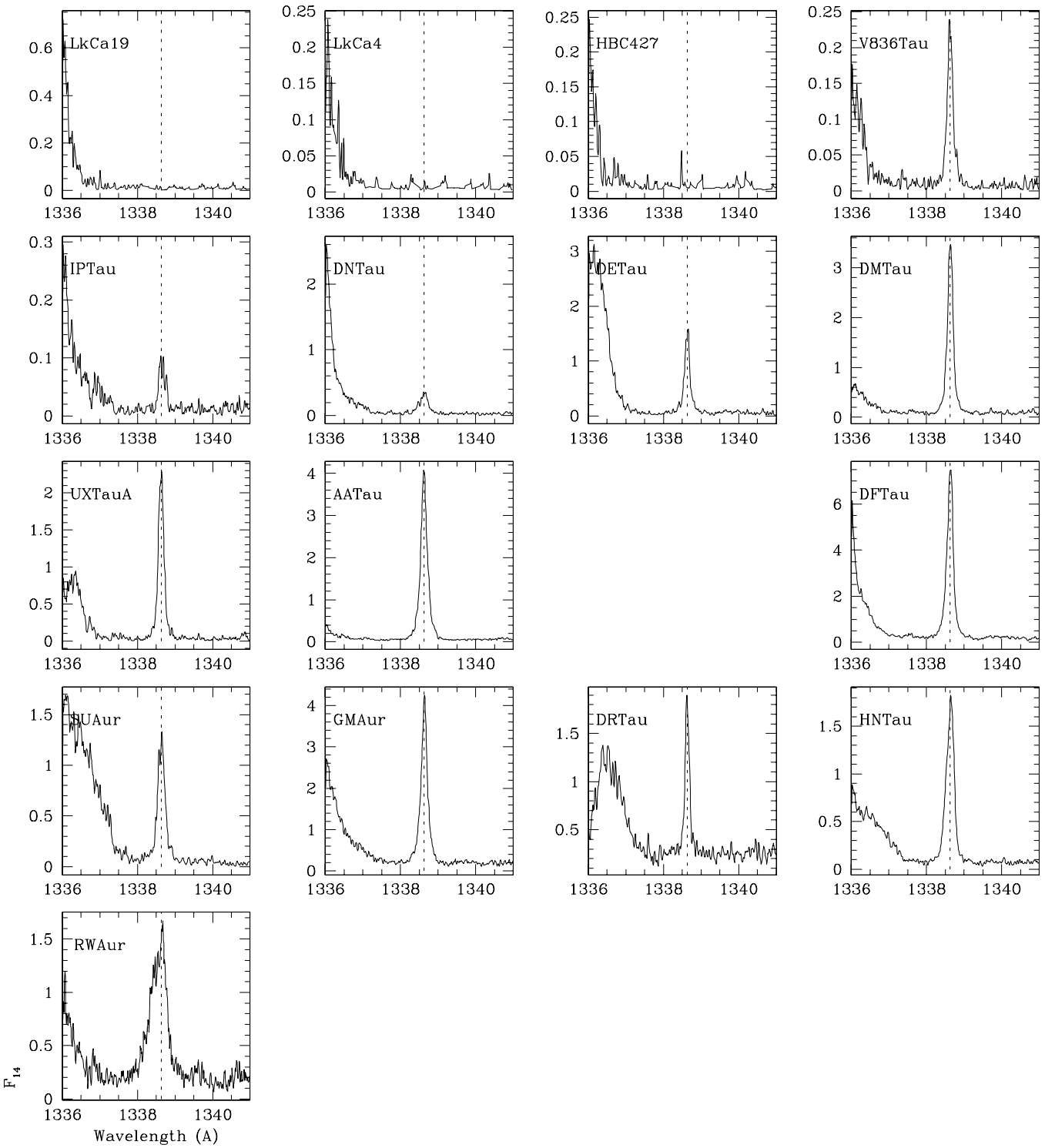

Figure 5. Profiles of the (P(2) 0–4) 1338.63 Å H_2 line of the TTSs studied in this work. The zero of the wavelength scale is set using H_2 lines for reference (see text). Notice the asymmetry and broadening of the RW Aur profile which prevent its use for this purpose. Fluxes are given in units of 10^{-14} erg s^{-1} cm^{-2} Å^{-1} (F_{14}).

unknown thickness but corrected for stellar radii and surface temperature. In this manner, the normalized fluxes compensate for scaling effects associated with the broad range of mass, luminosity, and stellar radius covered by the TTSs. Stars whose He II flux has a significant contribution from the LDC are marked in the plot. Notice that they are evenly distributed in the figure, which suggests that He II and N V fluxes are correlated regardless of whether the He II flux is dominated by the narrow emission component.

3.2. The Connection between UV and the X-Ray Radiation from the TTSs

Based on low resolution observations, GdCMA2012 pointed out that the normalized He II flux anti-correlates with the strength of the X-ray flux as derived in the XEST survey (Güdel et al. 2007) carried out with the *XMM-Newton* telescope in the 0.3–10.0 keV band. In Figure 10, the normalized He II fluxes from the high resolution COS/*HST* observation (see Table 3)

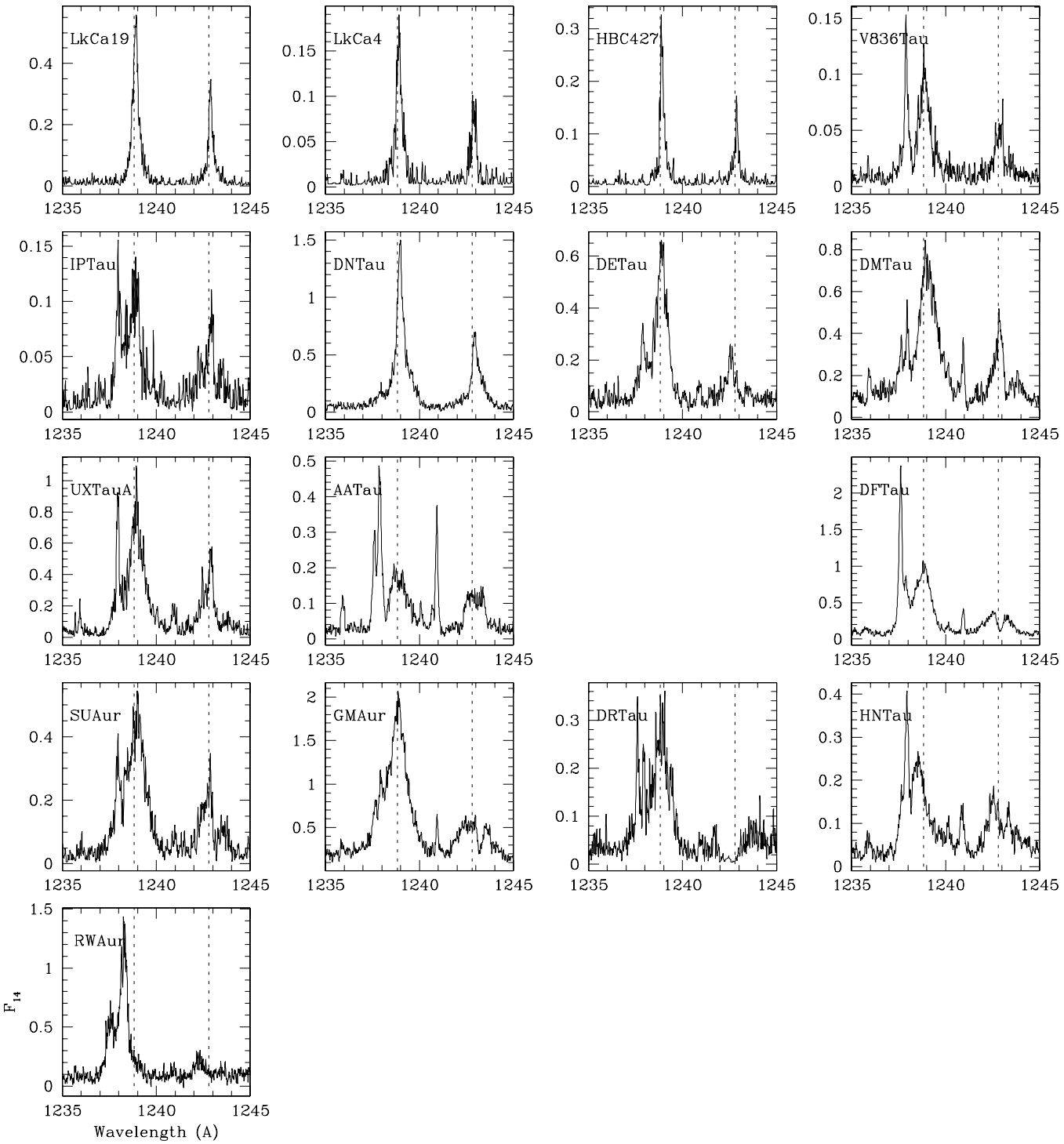

Figure 6. N v profiles of the TTSs in Taurus. The rest wavelengths of the N v lines are marked for reference (see also Figure 5). Fluxes are given in units of 10^{-14} erg s^{-1} cm^{-2} Å^{-1} (F_{14}).

are represented against the normalized X-ray luminosities as derived from the XEST survey. Also, the *Chandra*/ACIS observations of LkCa 4, DE Tau, and GM Aur from Yang et al. (2012) are used; they are integrated X-ray luminosities in the 0.3–10 keV range. The He II flux is extinction corrected according to Valencic et al. (2004), assuming $R = 3.1$ and the extinctions in Table 3. The low dispersion GdCMA2012 data also have been plotted for those sources with no available high dispersion data. A first inspection of Figure 10, shows three groups. The WTTSs (HBC 427, LkCa 4, HD283472), UX Tau, and the fast rotator SU Aur are very close to the main sequence stars regression line. The CTTSs follow the generic trend pointed out by GdCMA2012: the He II flux increases as the X-ray flux decreases. Notice that the sources with strong LDCs are far from this trend, excluding the fast rotator SU Aur. In fact, the Spearman rank correlation coefficient $r_s = -0.2622$ has $\alpha = 0.294$, with α being the level of significance, i.e., there is a probability of $\alpha = 0.294$ that the X-ray and He II normalized luminosities are not correlated (see Sachs 1982 for a detailed description of α for normal and non-normal error

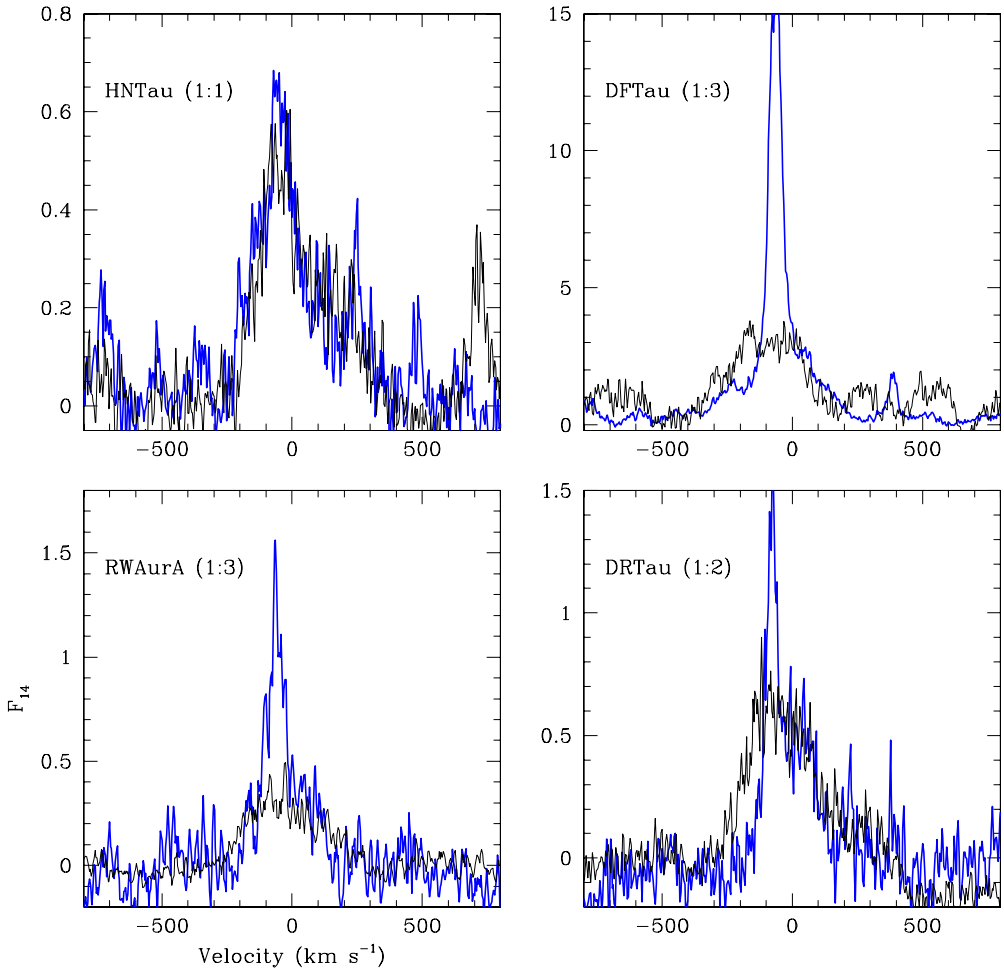

Figure 7. High S/N O III] profiles (black) over-plotted on the respective He II profiles (blue). The O III] profiles are re-scaled for comparison. The scaling factor is indicated in the figure for every profile.

(A color version of this figure is available in the online journal.)

distributions and the most usual statistical tests, including the Spearman rank correlation). However, if HN Tau, DE Tau, and DM Tau are excluded, the Spearman rank correlation coefficient is $r_s = -0.591$, with $\alpha = 0.033$, and the least square fit is

$$\log\left(\frac{F(L_X)}{F_{\rm bol}}\right) = (-0.20\pm0.05)\log\left(\frac{F({\rm He\,II})}{F_{\rm bol}}\right) - (4.3\pm0.2),$$

with rms = 0.15.

Given the uncertainties in the A_V values for the TTSs, it is worth evaluating whether the deviation from the general trend of the stars is caused by the uncertainties in the A_V values. To examine this effect, the same diagram has been plotted in the bottom panel of Figure 10, though this figure uses stellar luminosities, X-ray luminosities, and A_V values from the recent compilation by Yang et al. (2012). As shown, the three groups are not cleanly separated, and the regression line is more clear now. Moreover, only DE Tau is far from the trend. As a result, $r_s = -0.561$, with $\alpha = 0.036$, and

$$\log\left(\frac{F(L_X)}{F_{\rm bol}}\right) = (-0.17\pm0.07)\log\left(\frac{F({\rm He\,II})}{F_{\rm bol}}\right) - (4.1\pm0.1),$$

with rms = 0.15 (excluding DE Tau for these calculations).

In summary, though the clean separation between WTTSs and accreting TTSs may be an extinction associated effect, the trend to release preferentially the high energy excess in the UV rather than in the X-ray channel in accreting objects holds.

The current observations do not show *a statistically meaningful* deviation of the sources with strong LDCs from the main trend. Note also that the sample is small; there are not X-ray measurements of DR Tau or DF Tau, and RW Aur was detected to have a low soft X-ray flux only with the *Einstein* satellite (Damiani et al. 1995). If present, such a trend could indicate that X-ray radiation is dominated by different components in sources with strong LDCs (strong nebular component) and in sources with weak or absent LDCs. The X-ray energy distribution of the TTSs is often modeled by two components: a soft component at $T_s \simeq (2\text{–}5)10^6$ K and a hard component at $T_h \simeq (1.5\text{–}3)10^7$ K (see, i.e., Glassgold et al. 2000). The hard X-ray component is thought to be associated with magnetic energy release in the stellar coronae. The nature of the soft X-ray component is more uncertain, and it has often been hypothesized that it could be formed in accretion shocks (Lamzin 1998; Gullbring et al. 1998). Unfortunately, only three stars in our sample, namely, T Tau, SU Aur, and HBC 427, have a high enough count rate to allow a spectral fitting to two different optically thin plasmas. Only non-conclusive results could be derived from the fits (see Table 6 with the two-components fit to the X-ray spectrum of these sources—which is from Table 6 in Güdel et al.

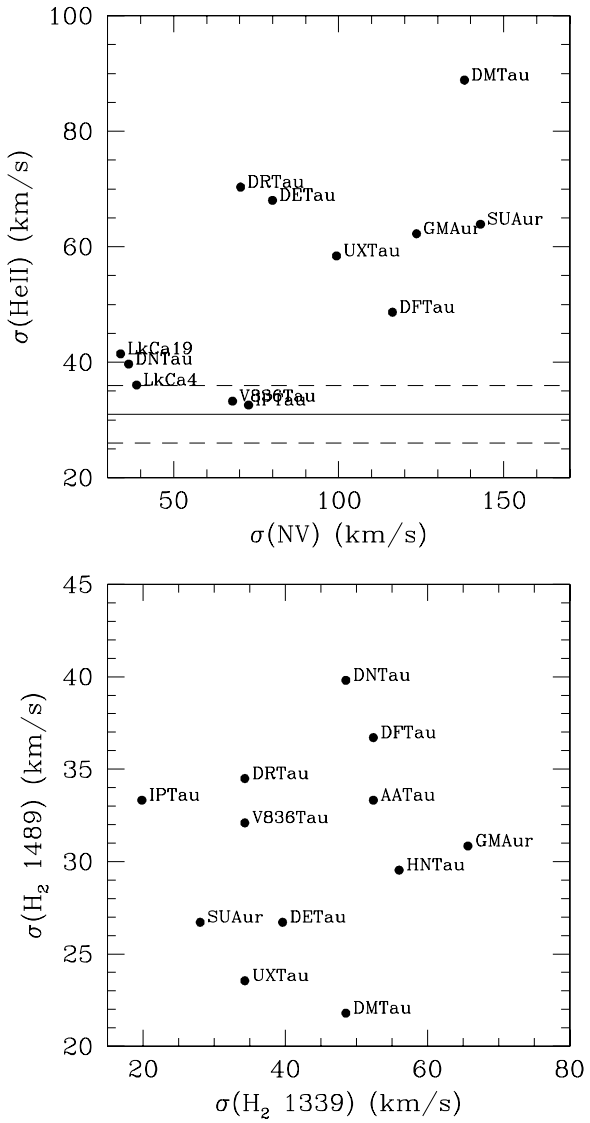

Figure 8. Top panel: broadening of the N v line (dispersion) compared with the broadening of the He ii line. The broadening is defined as the dispersion of the profile (see text). For comparison, the broadening of the H_2 1489 Å and 1389 Å lines are plotted in the bottom panel. The dispersion of the N v line is larger than that measured in the H_2 1389 Å line in all sources. However, the dispersion of H_2 1489 Å is comparable to that observed in the He ii line in WTTSs and transitional objects. The average σ (H_2 (1489)) $= 31 \pm 5$ km s^{-1} is represented in the top panel; the solid line represents the average; and the error band is marked with dashed lines. Circled sources have a significant LDC contribution to the He ii flux.

Table 6
Two Temperature Fits to the *XMM-Newton* Spectra from XEST

Star	T_1 (MK)	T_2 (MK)	EM_1 10^{52}	EM_2 10^{52}	EM_1/EM_2
T Tau	4.52	23.65	33.86	57.85	0.585
SU Aur	5.22	23.30	87.01	32.45	2.681
HBC 427	9.04	28.06	14.98	15.07	0.994

2007). The X-ray spectrum of SU Aur, a CTTS, is dominated by the low temperature component with $T = 5.22$ MK. However, both the soft and hard X-ray components have similar emission measures in HBC 427, a non-accreting WTTSs. Moreover, the hard X-ray component dominates the X-ray spectrum of the CTTS, T Tau.

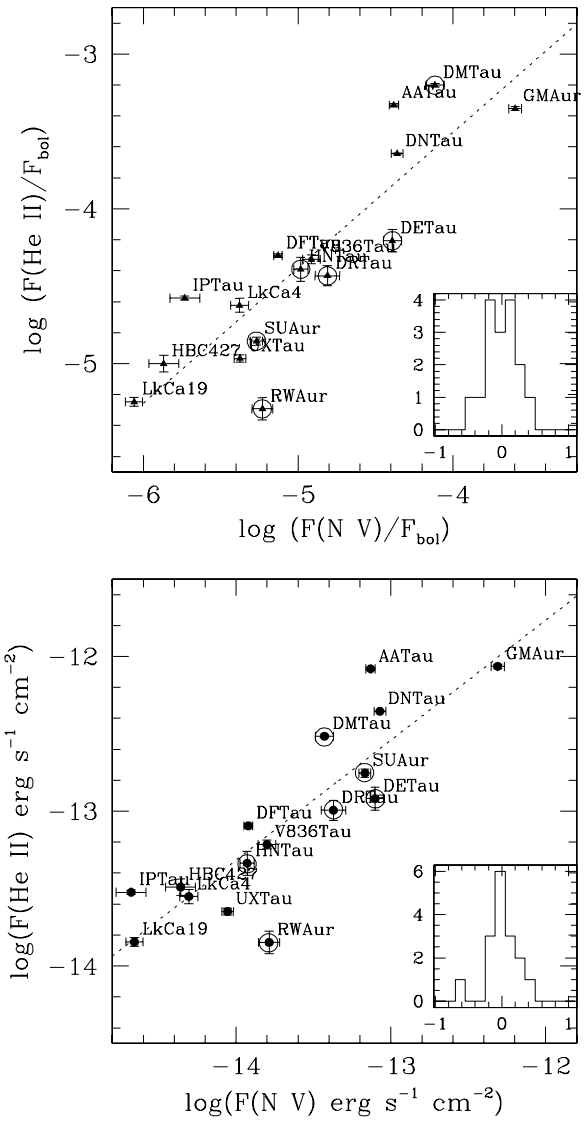

Figure 9. Bottom: the He ii flux is plotted vs. the N v flux. Top: the He ii normalized flux is plotted against the N v normalized flux. Fluxes are extinction corrected. The small insets at the bottom-right corner are the histograms representing the distance of the sources from the main regression line, plotted as a dashed line. Circled sources have significant LDC contributions to the He ii flux.

4. DISCUSSION

TTSs are complex objects. They are convective PMS stars where a solar-like dynamo begins to set in while the fossil magnetic field is still diffusing. TTSs are surrounded by an external dynamo that powers and makes the stellar magnetosphere rise to the inner border of the molecular disk (see Romanova et al. 2012 for recent simulations). Matter from the disk slides down onto the star along the magnetospheric field lines to end, free-falling onto the open holes of the magnetic configuration. In this environment, hot plasma radiating in the UV tracers studied in this work can be located in the magnetosphere, in the atmosphere, in the accretion shocks, and also in the outflow (either solar-like or driven from the star–disk magnetic interface or the disk). Within the current paradigm, both the magnetosphere and the outflow have significantly lower densities than the stellar atmosphere or the accretion shocks. As a result, spectral line radiation is dominated by

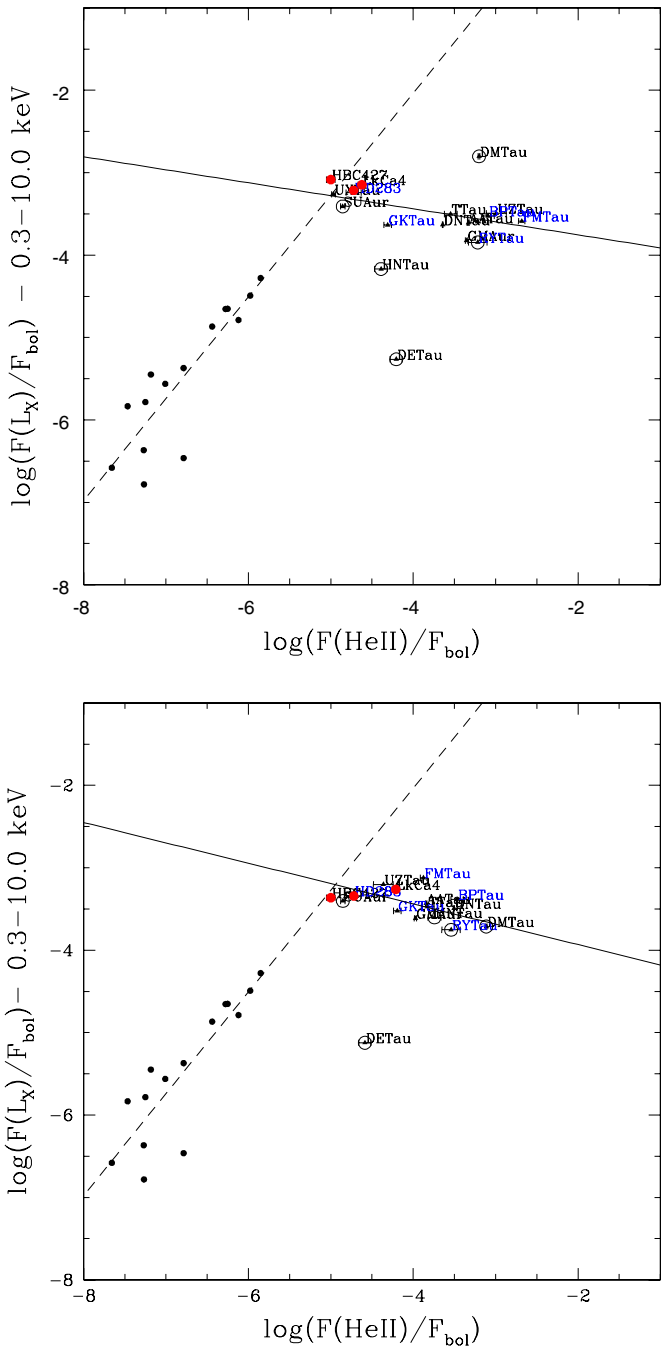

Figure 10. Normalized X-ray flux vs. normalized He II flux for TTSs compared with main sequence cool stars (MSCSs). TTSs are plotted with triangles and the error bars are marked. MSCSs are plotted with filled circles (data from Ayres et al. 1995 and Linsky et al. 1982, as described in GdCMA2012). The MSCSs' regression line is plotted with a dashed line and the TTSs' regression line with a continuous line. The stars names are indicated in black for F (He II) measurements based on high resolution data (this work) and in blue for GdCMA2012 measurements based on low dispersion data. Red dots mark the location of the WTTSs. Top: A_V, f_{bol}, and L_X, as in Table 3. Circled sources have significant LDC contributions to the He II flux. Bottom: A_V, f_{bol}, and L_X, as in Table 2 of Yang et al. (2012).

(A color version of this figure is available in the online journal.)

radiative de-excitation processes, and forbidden and semiforbidden transitions are strong from this plasma. In the dense atmosphere, collisional de-excitation is relevant, and forbidden transitions are expected to be quenched. UV semiforbidden transitions cannot be observed from the accretion shock itself because it is too hot and dense. However, the soft X-ray radiation produced in the shock front photoionizes the preshock gas, which has a density similar to that of the stellar magnetosphere and may produce forbidden line radiation (Gómez de Castro & Lamzin 1999). Unfortunately, the high column density prevents the UV radiation from the photoionization cascade to escape easily from the accretion column. Also, the profiles of some tracers, from the infrared He I transition (Beristain et al. 2001; Fischer et al. 2008) to the UV lines, do not agree with the predictions of accretion shock models (Johns-Krull 2009). Within this context, the data presented in Section 3 provide some amazing results:

1. The He II, O III], and N V fluxes do not depend on the spectral type. This confirms that *the line emission is not dominated by main sequence like atmospheric magnetic activity*, i.e., with the release of the magnetic energy produced by the stellar dynamo, since this one depends on the spectral type (see, e.g., Ayres et al. 1995; GdCMA2012).
2. The He II and N V fluxes correlate well regardless of whether the line profiles are very different, e.g., independently of whether the line emission is produced in the same physical structure. This confirms that all processes (accretion, atmospheric emission, and outflow) are coupled, as expected (see Gómez de Castro 2013 for a recent review). In turn, it makes difficult to obtain specific tracers of individual processes without kinematical information, i.e., without high resolution spectroscopy.
3. The high resolution profiles of the N V line show a symmetric line broadening that increases from non-accreting to accreting stars, being significantly suprathermal in these last sources (see Table 5). The profile shape and the density of the line formation region suggests an atmospheric origin (with the exceptions already mentioned in Section 3). The connection between line broadening and accretion suggests that the density and extent of the high atmospheric layers depends on the accretion rate, i.e., on the evolutionary state, as otherwise predicted from the theoretical models (D'Antona & Mazzitelli 1997; Siess et al. 2000). Transport of magnetic energy from the stellar interior to the surface is expected to occur at a different pace in accreting sources than in WTTSs. Moreover, the extended magnetosphere powered by the disk–star magnetic locking, must affect the stellar atmosphere introducing new sources of stirring and turbulence (see, e.g., Kivelson & Russell 1995).
4. The physical source of the narrow emission component in the He II profile, however, remains uncertain. It could either be associated with accretion shocks or with atmospheric features.

In this section, the possible source of the He II narrow emission component is analyzed, and some constraints on the extent of the magnetosphere are inferred from the semiforbidden line radiation.

4.1. On the Source of the Narrow Component of the He II Line: Accretion Shocks or Bulk Atmospheric Phenomena?

The kinematics of the region where the narrow component forms, is clearly distinct from that of the N V or the O III] lines formation region (see Figure 8). The dispersion of the narrow emission component of the He II ranges from ∼20 km s^{-1} to ∼60 km s^{-1}, while the dispersion of the N V line varies from ∼40 km s^{-1} to ∼130 km s^{-1} for the same sources (see Figure 11). The dispersion of the narrow emission component in

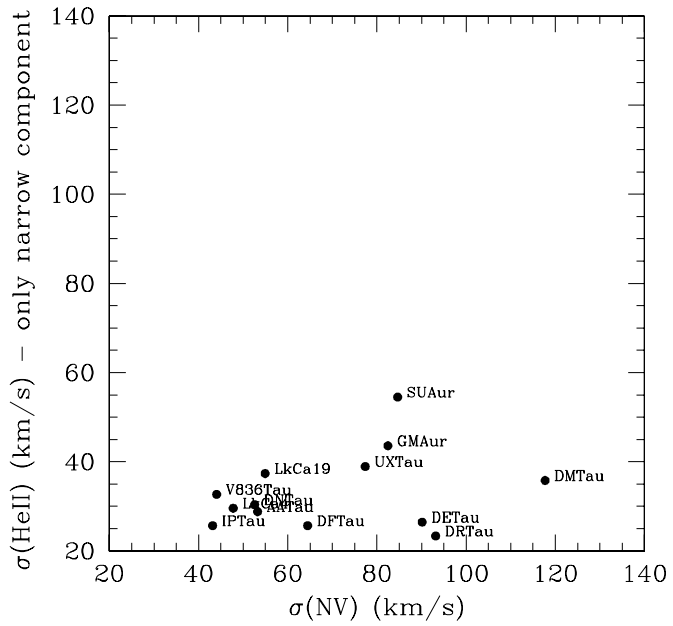

Figure 11. Same as Figure 8, except that the dispersion of the He II line is evaluated only for the narrow component of the profile.

the He II profile has been evaluated as above (see Section 3) but for setting an upper wavelength cut-off to reject the contribution of the LDC. Note that even in setting this cut-off, there is an unknown contribution from the LDC to the flux.

Moreover, the narrow component seems to be slightly redshifted in *all* sources, from 24 km s^{-1} in UX Tau to 37 km s^{-1} in DE Tau (see the Appendix and Table 7). Hence, it would be tempting to suggest that the line is produced in accretion shocks.

Accretion shocks are produced by the impact of the free-falling material from the disk onto the stellar surface. The kinetic energy of the infalling matter, with typical free-fall speeds of ∼300 km s^{-1}, is involved in gas heating at the shock front that reaches temperatures of about 1 MK. The soft X-ray radiation from the shock front is expected to photoionize (pre-ionize) the infalling gas column (see, i.e., Lamzin 1998; Gómez de Castro & Lamzin 1999; Muzerolle et al. 2001; Orlando et al. 2009). Also, the shock front could back illuminate the stellar surface, becoming a source of atmospheric photoionization to be added to the coronal X-ray radiation. In this context, the narrow component of the He II line could be produced very close to the shock front. The slight, but small redshift, could be interpreted as an indication of the line being formed in postshock material, and the small width could be caused by thermal broadening. The thermal velocity of fully ionized, solar abundance plasma at 50,000 K is 23 km s^{-1}. However, this cannot be concluded from these data alone. Firstly, the apparent redshift could be caused by the blending of the narrow component with the broad component, which is asymmetric in most sources, e.g., with very low or absent flux at blueward-shifted velocities. The line broadening is affected by the same problem, though no so dramatically given the relative strengths of the narrow and broad components. Unfortunately, unless very high S/N profiles (∼100) of the semiforbidden and the He II lines are obtained, any fitting is hampered by these uncertainties. Finally, it is also, intriguing that the broadening of the He II emission line in non-accreting TTSs, such as LkCa 4, LkCa 19, and HBC 427, is comparable to that observed in UX Tau or in V836 Tau, which are TTSs with low accretion rates. In this respect, it is worth noticing that the correlation between the He II flux and the accretion luminosity, as derived from the *U*-band excess (Ingleby et al. 2009; Gullbring et al. 1998), is mild,[4] as shown in Figure 12 (see also GdCMA2012).

Table 7
Shift of the He II Narrow Emission Component

Stars	$\Delta\lambda = \lambda_{peak} - \lambda_0$ (Å)
AA Tau	0.175
DE Tau	0.202
DF Tau	0.188
DM Tau	0.166
DN Tau	0.164
DR Tau	0.115
GM Aur	0.186
IP Tau	0.151
UX Tau	0.13
V836 Tau	0.166

Taking into account all these facts, as well as the good correlation between the He II and the N V fluxes (Figure 9) and the convergence of the He II and N V line broadenings toward the non-accreting WTTSs, a contribution to the narrow component of the He II line from the stellar atmosphere cannot be neglected. For all the reasons mentioned above, it is most probable that both physical components, accretion shocks and the stellar atmosphere, contribute to the flux.

4.2. Properties of the LDC

The profiles produced in the LDC cannot be ascribed to simple kinematics shared by all sources, neither can the radiating plasma be modeled by simple collisional plasma models. However, some constraints on its overall physical properties can be derived from the ratios of the intercombination lines of O III], Si III], and C III]. The plasma density can be constrained from the Si III]/C III] ratio (Gómez de Castro & Verdugo 2001). The detection of O III] can be used to fix up the temperature since the O III]/Si III] ratio is very sensitive to it.

The Si III] and C III] lines have been observed with STIS for three sources in the sample: RW Aur (Gómez de Castro & Verdugo 2003, hereafter GdCV2003), DE Tau, and T Tau (Gómez de Castro et al. 2003). T Tau profiles display a non-negligible contribution from the large scale jet. DE Tau Si III] and C III] profiles are rather narrow and similar to the O III] line. From studying RW Aur, GdCV2003 pointed out that the emitting volume is clumpy with a rather small filling factor, as expected if magnetospheric radiation is produced in plasma filaments and clumps. This clumpy nature, together with the broad temperature range covered by the various spectral tracers, suggests that the excitation mechanism could be photoionization instead of collisional excitation.

GdCV2003, making use of CLOUDY (Ferland 1996), a code designed to simulate emission line regions in astrophysical

[4] Note that the He II flux and the accretion luminosity measurements are not simultaneous. However, the variability of the He II flux and, in general, of the UV tracers (continuum lines) is typically smaller than a factor of two (Gómez de Castro et al. 1997; Huélamo et al. 2000). Measurements of the accretion rate are based on the *U*-band excess that also typically varies by this amount (Gullbring et al. 1998).

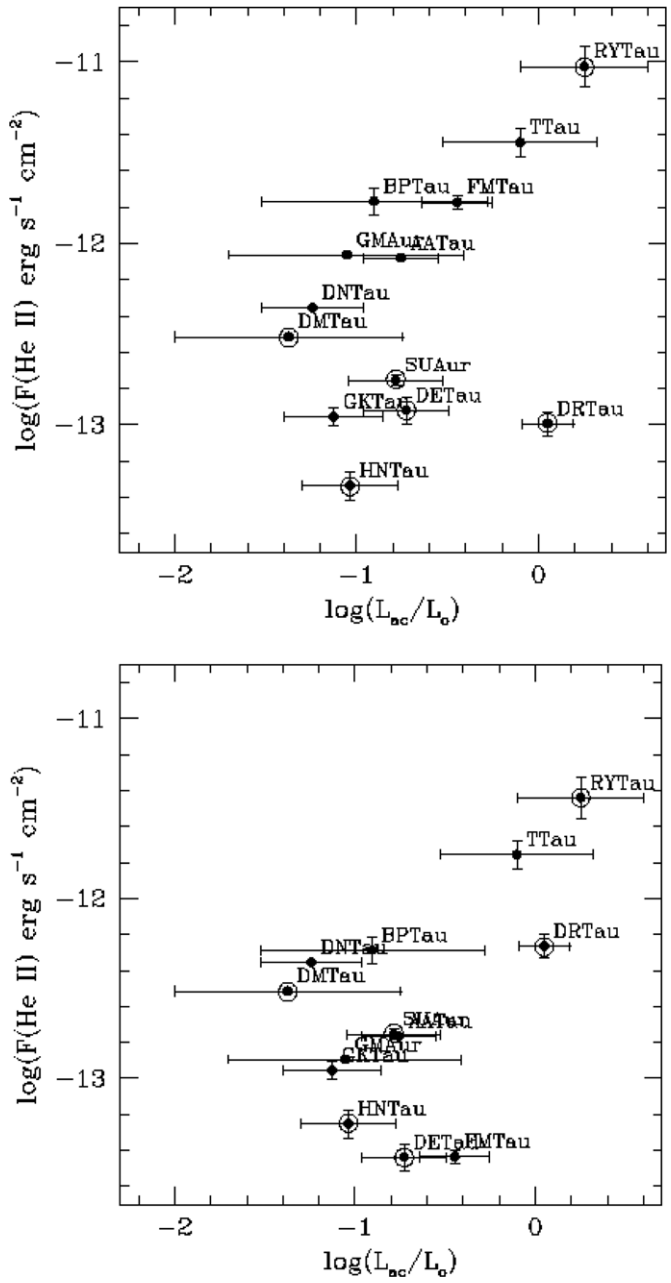

Figure 12. Top panel: He II fluxes vs. accretion luminosities using extinctions from Table 3. Bottom panel: same as the top panel but with extinctions from Yang et al. (2012). Note that accretion luminosities have not been measured simultaneously; typical variations can account for a factor as large as ∼2 (0.3 in logarithmic scale).

environments, produced two grids of photoionization models to explore possible regimes for line excitation. The first set assumed that LDC had a belt-like geometry, being illuminated by the ambient X-ray radiation field: soft and hard components, at 3.5×10^6 K and 2.8×10^7 K, respectively, with a total X-ray luminosity of 3×10^{29} erg s^{-1}. This model turned out to be unable to reproduce comparable strengths of the three spectral tracers. However, if the O III], Si III], and C III] emission is assumed to be produced in dense gas around small X-ray sources, such as reconnecting loops, the line ratios could be reproduced for electron densities of $n_e \geqslant 10^{11}$ cm^{-3}. For soft X-ray sources with $T_e = 10^6$ K, luminosities of 10^{27} erg s^{-1}, and radii of 10^8 cm^{-3}, the inferred O III] emissivity is $\sim 10^{-3.5}$ erg s cm^{-2}. Using this as a fiducial value or an estimate of the LDC volume, $V_{\rm LDC}$ could be derived from the line strength as $(V_{\rm LDC}/\eta) = (F({\rm O\,III}])4\pi d^2/\epsilon_{O\,{\rm III}]})$, where F(O III]) is the reddening corrected line flux and η is the filling factor of the hot plasma. For filling factors of 10%, and assuming that the emission is concentrated in a spherical shell of radius $R_{\rm LDC}$ and thickness $0.01 R_{\rm LDC}$, LDC radii from 4 to 9 $R_{\odot}$ are inferred. These values are within a factor of 1.5 of the magnetospheric radii derived from accretion luminosities for stars with known magnetic fields (Johns-Krull 2007; GdCMA2012). Unfortunately, the uncertainties in the plasma distribution prevent more detailed evaluations.

5. CONCLUSIONS

The UV radiation from N V, He II, and O III] is dominated by the contribution of three main components of the TTSs atmospheric/magnetospheric environment: the magnetospheric flow of infalling matter, the disturbed upper atmospheric layers, and the accretion shock.

The diffuse magnetospheric plasma (LDC) is best traced by the O III] line: it produces asymmetric profiles, preferentially redshifted. The He II emission is observed from the same kinematical structures that radiate in O III]. There are indications that photoionization processes could be significant in the excitation of this plasma.

The hot, dense layers of the cool stars' atmospheres are best traced by the N V line. However, the line dispersion increases steadily from WTTSs to CTTSs, suggesting a connection between the line formation region and the accretion flow.

The He II flux is dominated by a narrow emission component of uncertain origin. In this work, we have presented evidence indicating that it may be formed in hot postshock material in accretion shocks, but we have also presented evidence of its connection with atmospheric tracers. Both accretion shocks, and the upper atmospheric layers seem to contribute to the narrow component of the He II profile.

The anticorrelation between X-ray and UV flux found by GdCMA2012 has been confirmed, suggesting that the dissipation of magnetic energy proceeds in the TTSs differently than in main sequence stars. The denser environment produced by mass accretion (see, i.e., Petrov et al. 2011) seems to favor the UV channel for the dissipation of the magnetic energy excess.

All the observations indicate that the UV radiation field during PMS evolution is much harder than that usually implemented in the modeling of protostellar disk evolution. An example of its effect in the dust grain charging and charging profile can be found in Pedersen & Gómez de Castro (2011). Theoretical modeling of protostellar disk chemistry and life generation environments should take this fact into account.

Kevin France brought to my attention the *HST*/COS data corresponding to AA Tau. The analysis of the data pointed out that the 1640 Å jump in the *HST*/ACS data was dominated by an unexpectedly strong He II line. This article has grown from extending this analysis to the TTSs observed with *HST*/COS. I would like to thank an anonymous referee for suggesting the use of the H_2 lines to set the zero of the wavelength scale. This work has been partly funded by the Ministerio de Economia y Competitividad of Spain through grant AYA2011-29754-C03-C01.

Facilities: HST (COS, STIS), XMM (EPIC)

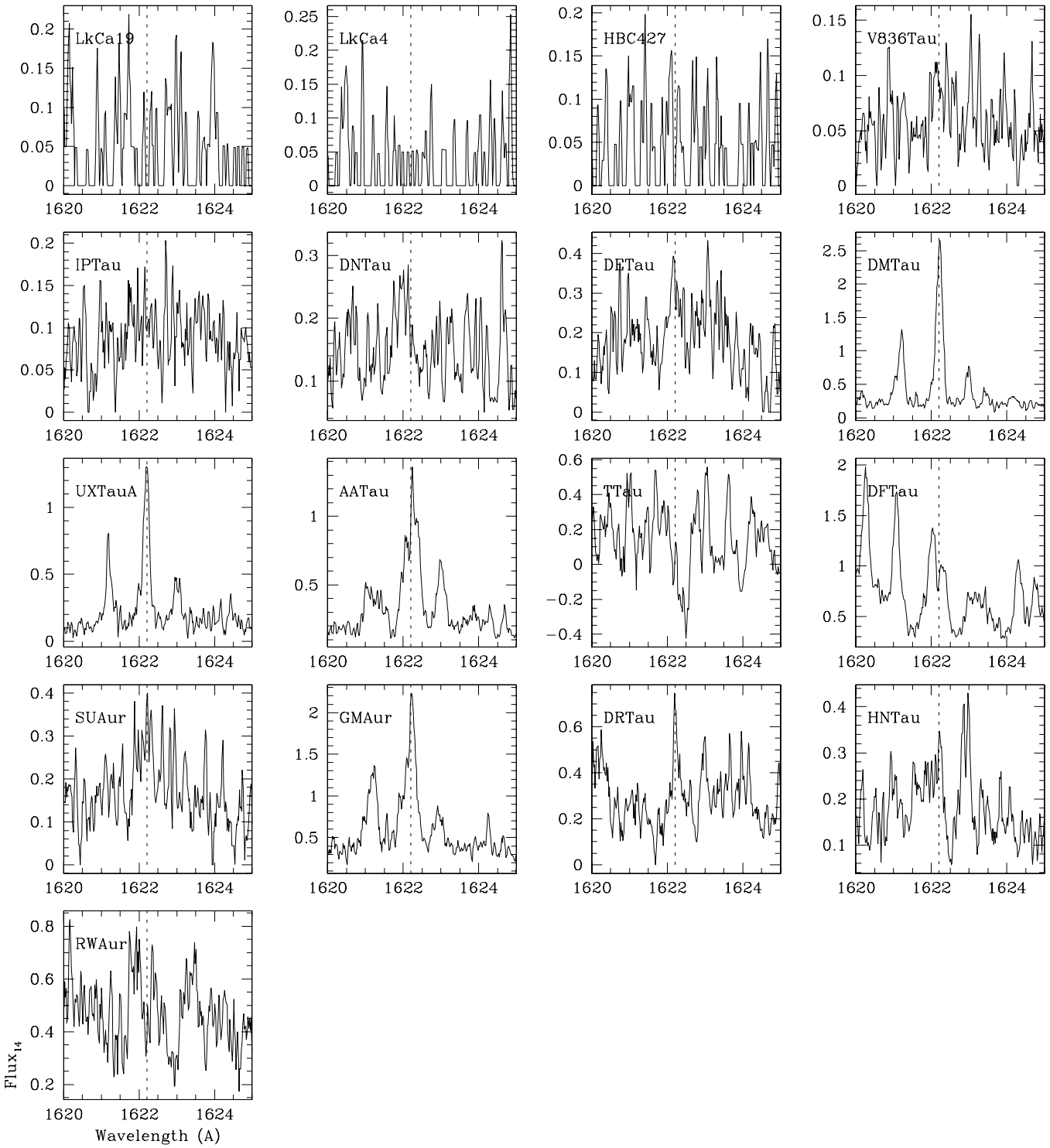

Figure 13. P(17)3–9 H_2 profiles of the TTSs in Taurus observed with *HST*. The rest wavelength is marked for reference. Fluxes are given in units of 10^{-14} erg s^{-1} cm^{-2} Å^{-1} (F_{14}).

APPENDIX

THE VELOCITY OF THE He II NARROW EMISSION COMPONENT

The narrow emission component of the He II line seems to be systematically redshifted with respect to the H_2 lines. The shifts are small (∼0.16 Å or 29 km s^{-1}), as shown in Table 7. The zero of the wavelength scale has been set with the (R(3) 1–7) 1489.636 Å and (P(5) 1–7) 1504.845 Å H_2 lines because they were observed in most of the stars. These lines are far from the 1640 Å He II line, and in principle, small uncertainties in the wavelength calibration could drive to these shifts. However, as shown in Figures 13 and 14, this is not the case. The P(17)3–9 line is plotted for the whole sample in Figure 13, though only is clearly observed in DM Tau, UX Tau A, AA Tau, GM Aur, and DR Tau (the H_2 emission from RW Aur cannot be used for this purpose). In all cases, the H_2 transition is at rest. In Figure 14, the C I [uv1] multiplet is plotted. It is observed as

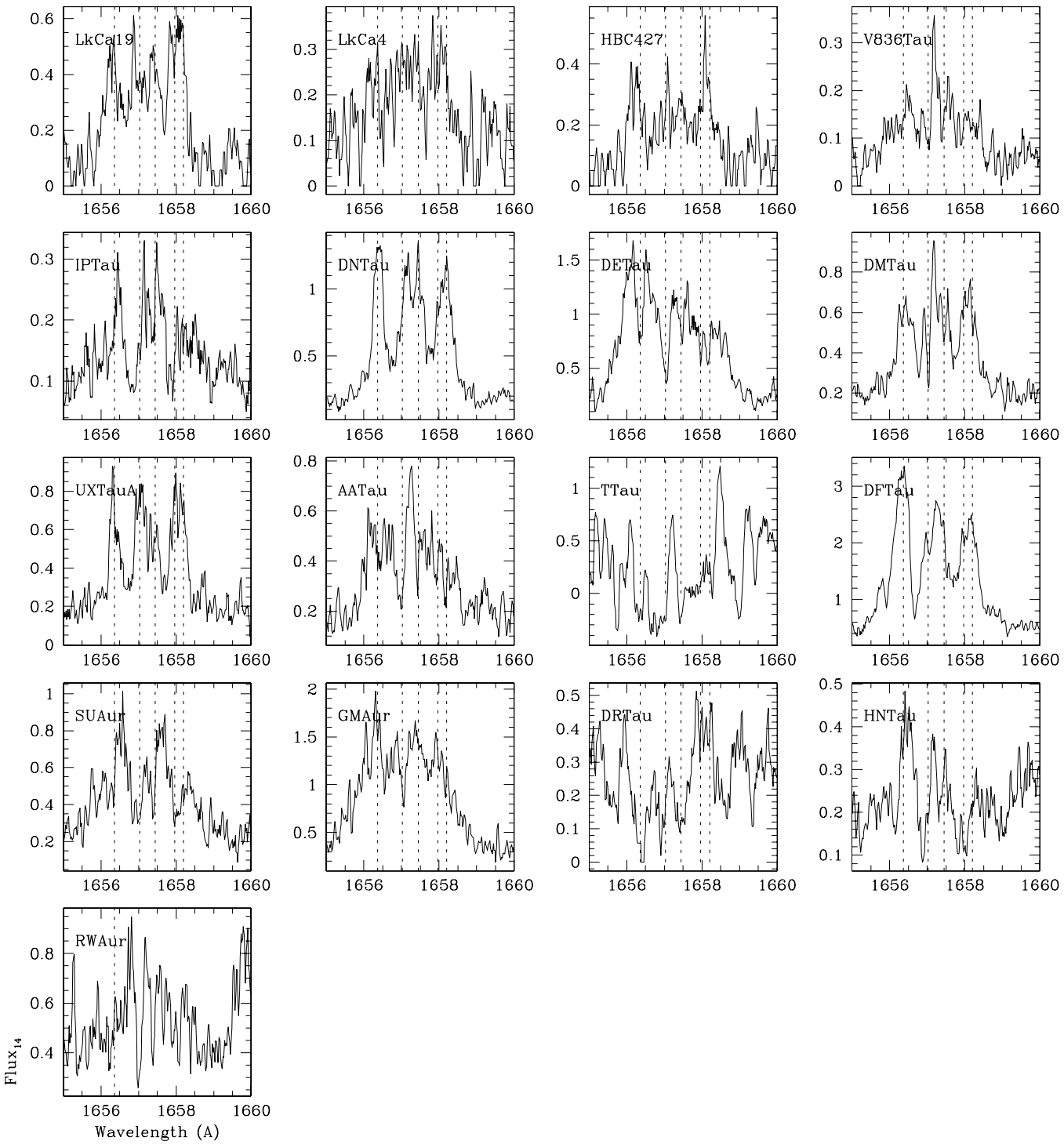

Figure 14. C I [uv1] profiles of the TTSs in Taurus observed with *HST*. The rest wavelength of the lines in the multiplet is marked for reference. Fluxes are given in units of 10^{-14} erg s^{-1} cm^{-2} Å^{-1} (F_{14}).

narrow emission lines in DN Tau, DM Tau, UX Tau A, and DF Tau. In all cases, the lines are at rest wavelength. This redshift is observed both in CTTSs and intermediate objects (it cannot be measured in WTTSs because of the lack of H_2 emission). Thus, unless the P(14) 3–10 H_2 transition, which is blended with the He II line, is unusually strong, it must be concluded that the narrow emission component of the He II line is redshifted in most sources. However, note that the blending with the broad component could produce an apparent redshift if this broad component is asymmetric.

REFERENCES

Ardila, D. R., Basri, G., Walter, F. M., et al. 2002, ApJ, 566, 1100
Ayres, T. R. 2005, in Proc. 13th Cambridge Workshop on Cool Stars, Stellar Systems and the Sun, ed. F. Favata, G. A. J. Hussain, & B. Battrick (ESA-SP 560; Hamburg: European Space Agency), 419
Ayres, T. R., Fleming, T. A., Simon, T., et al. 1995, ApJS, 96, 223
Beristain, G., Edwards, S., & Kwan, J. 2001, ApJ, 551, 1037
Bertout, C., Siess, L., & Cabrit, S. 2007, A&A, 473, L21
Clarke, C. J., & Bouvier, J. 2000, MNRAS, 319, 457
D'Antona, F., & Mazzitelli, I. 1997, MmSAI, 68, 807
Damiani, F., Micela, G., Sciortino, S., et al. 1995, ApJ, 446, 331

Ferland, G. J. 1996, Hazy, a Brief Introduction to Cloudy, Internal Report, Department of Physics and Astronomy, Univ. Kentucky
Fischer, W., Kwan, J., Edwards, S., et al. 2008, ApJ, 687, 1117
France, K., Schindhelm, E., Herczeg, G. J., et al. 2012, ApJ, 756, 171
Glassgold, A. E., Feigelson, E. D., & Montmerle, T. 2000, in Protostars and Planets IV, ed. V. Mannings, A. P. Boss, & S. S. Russell (Tucson, AZ: Univ. Arizona Press), 429
Gómez de Castro, A. I. 2013, in Planets, Stars and Stellar Systems, ed. T. D. Oswalt, I. S. McLean, H. E. Bond, L. French, P. Kalas, M. A. Barstow, G. F. Gilmore, & W. C. Keel (Berlin: Springer), 279
Gómez de Castro, A. I., & Ferro-Fontán, C. 2005, MNRAS, 362, 569
Gómez de Castro, A. I., Franqueira, M., & Wamsteker, W. 1997, International Ultraviolet Explorer - Uniform Low Dispersion Archive: T Tauri Stars (IUE-ULDA access guide no. 8; Noordwijk: ESA)
Gómez de Castro, A. I., & Lamzin, S. 1999, MNRAS, 304, L41
Gómez de Castro, A. I., López-Santiago, J., Talavera, A., et al. 2013, ApJ, 766, 62
Gómez de Castro, A. I., & Marcos-Arenal, P. 2012, ApJ, 749, 190
Gómez de Castro, A. I., & Verdugo, E. 2001, ApJ, 548, 976
Gómez de Castro, A. I., & Verdugo, E. 2003, ApJ, 597, 443
Gómez de Castro, A. I., & Verdugo, E. 2007, ApJL, 654, L91
Gómez de Castro, A. I., Verdugo, E., & Ferro-Fontán, C. 2003, in 12th Cambridge Workshop on Cool Stars, Stellar Systems, and the Sun, The Future of Cool-Star Astrophysics, ed. A. Brown, G. M. Harper, & T. R. Ayres (Boulder, CO: Univ. Colorado), 40
Gómez de Castro, A. I., & von Rekowsky, B. 2011, MNRAS, 411, 849
Green, J. C., Froning, C. S., Osterman, S., et al. 2012, ApJ, 744, 60
Güdel, M., Briggs, K. R., Arzner, K., et al. 2007, A&A, 468, 353
Guenther, E. W., Lehman, H., Emerson, J. P., & Staude, J. 1999, A&A, 341, 768
Gullbring, E., Hartmann, L., Briceno, C., et al. 1998, ApJ, 492, 323
Hartmann, L. 2009, in Protostellar Jets in Context, ed. K. Tsinganos, T. Ray, & M. Stute (Astrophysics and Space Science Proceedings Series; Berlin: Springer), 23
Hartmann, L., Avrett, E., & Edwards, S. 1982, ApJ, 261, 279
Herczeg, G. J., Linsky, J. L., & Valenti, J. A. 2002, ApJ, 572, 310
Hirth, G. A., Mundt, R., & Solf, J. 1997, A&AS, 126, 437
Huélamo, N., Franqueira, M., & Gómez de Castro, A. I. 2000, MNRAS, 312, 833
Huélamo, N., Gómez de Castro, A. I., & Franqueira, M. 1998, in Ultraviolet Astrophysics Beyond the IUE Final Archive, ed. B. Harris (ESA-SP 413; Noordwijk, The Netherlands: ESA Publications Division), 121
Ingleby, L., Calvet, N., Bergin, E., et al. 2009, ApJL, 703, L137
Johns-Krull, C. M. 2007, ApJ, 664, 975
Johns-Krull, C. M. 2009, in Protostellar Jets in Context, ed. K. Tsinganos, T. Ray, & M. Stute (Astrophysics and Space Science Proceedings Series; Berlin: Springer), 33
Johns-Krull, C. M., Valenti, J. A., & Koresko, C. 1999, ApJ, 516, 900
Johns-Krull, C. M., Valenti, J. A., & Linsky, J. L. 2000, ApJ, 539, 815
Johns-Krull, C. M., Valenti, J. A., & Saar, S. H. 2004, ApJ, 617, 1204
Kenyon, S. J., & Hartmann, L. 1995, Ap&SS, 101, 117
Kivelson, M. G., & Russell, C. T. (ed.) 1995, in Introduction to Space Physics (Cambridge: Cambridge Univ. Press), 330
Kriss, G. A. 2011, Improved Medium Resolution Line Spread Functions for COS FUV Spectra, Technical Report
Lamzin, S. 1998, ARep, 42, 322
Lemmens, A. F. P., Rutten, R. G. M., & Zwaan, C. 1992, A&A, 257, 671
Lima, G. H. R. A., Alencar, S. H. P., Calvet, N., et al. 2010, A&A, 522, 104L
Linsky, J. L., Bornmann, P. L., Carpenter, K. G., et al. 1982, ApJ, 260, 670
Muzerolle, J., Calvet, N., & Hartmann, L. 2001, ApJ, 550, 994
Orlando, S., Sacco, G. G., Argiroffi, C., et al. 2009, A&A, 510, 71
Pedersen, A., & Gómez de Castro, A. I. 2011, ApJ, 740, 77
Penston, M., & Lago, M. T. V. T. 1983, MNRAS, 202, 77
Petrov, P. P., Gahm, G., F., Stempels, H. C., et al. 2011, A&A, 535, 6
Romanova, M. M., Ustyugova, G. V., Koldoba, A. V., et al. 2004, ApJ, 610, 920
Romanova, M. M., Ustyugova, G. V., Koldoba, A. V., et al. 2012, MNRAS, 421, 63
Sachs, L. 1982, Applied Statistics: A Handbook of Techniques (Springer Series in Statistics; New York: Springer)
Siess, L., Dufour, E., & Forestini, M. 2000, A&A, 358, 593
Valencic, L. A., Clayton, G. C., & Gordon, K. D. 2004, ApJ, 616, 912
Yang, H., Herczeg, G. J., Linsky, J. L., et al. 2012, ApJ, 744, 121